









Site-specific functionality and tryptophan mimicry of lipidation in tetraspanin CD9

Viviana Neviani¹ , Sjoerd van Deventer² , Tobias P. Wörner³, Katerina T. Xenaki⁴ , Michiel van de Waterbeemd³, Remco N. P. Rodenburg¹, Inge M. N. Wortel² , Jeroen K. Kuiper², Sofie Huisman¹, Joke Granneman¹, Paul M. P. van Bergen en Henegouwen⁴ , Albert J. R. Heck³ , Annemiek B. van Spriel²  and Piet Gros¹ 

¹ Crystal and Structural Chemistry, Department of Chemistry, Bijvoet Center for Biomolecular Research, Utrecht University, The Netherlands

² Department of Tumor Immunology, Radboud Institute for Molecular Life Sciences, Radboud UMC, Nijmegen, The Netherlands

³ Biomolecular Mass Spectrometry and Proteomics, Department of Chemistry, Bijvoet Center for Biomolecular Research and Utrecht Institute for Pharmaceutical Sciences, Utrecht University, The Netherlands

⁴ Cell Biology, Department of Biology, Utrecht University, The Netherlands

Keywords

CD9; lipidation; palmitoylation; tetraspanin; tryptophan mimicry

Correspondence

A. B. van Spriel, Department of Tumor Immunology (278), Radboud Institute for Molecular Life Sciences, P.O.Box 9101, 6500 HBNijmegen, The Netherlands
 Tel: +31-24-3617600

Email: annemiek.vanspriel@radboudumc.nl and

P. Gros, Crystal and Structural Chemistry, Department of Chemistry, Bijvoet Center for Biomolecular Research, Utrecht University, 3584 CH Utrecht, The Netherlands
 Tel: +31-30-2533127

E-mail: p.gros@uu.nl

Viviana Neviani, Sjoerd van Deventer, and Tobias P. Wörner contributed equally

(Received 4 November 2019, revised 19 January 2020, accepted 13 March 2020)

doi:10.1111/febs.15295

Lipidation of transmembrane proteins regulates many cellular activities, including signal transduction, cell–cell communication, and membrane trafficking. However, how lipidation at different sites in a membrane protein affects structure and function remains elusive. Here, using native mass spectrometry we determined that wild-type human tetraspanins CD9 and CD81 exhibit nonstochastic distributions of bound acyl chains. We revealed CD9 lipidation at its three most frequent lipidated sites suffices for EWI-F binding, while cysteine-to-alanine CD9 mutations markedly reduced binding of EWI-F. EWI-F binding by CD9 was rescued by mutating all or, albeit to a lesser extent, only the three most frequently lipidated sites into tryptophans. These mutations did not affect the nanoscale distribution of CD9 in cell membranes, as shown by super-resolution microscopy using a CD9-specific nanobody. Thus, these data demonstrate site-specific, possibly conformation-dependent, functionality of lipidation in tetraspanin CD9 and identify tryptophan mimicry as a possible biochemical approach to study site-specific transmembrane-protein lipidation.

Abbreviations

DBSCAN, density-based spatial clustering analysis; DDM, *n*-dodecyl β -D-maltopyranoside; dSTORM, direct stochastic optical reconstruction microscopy; EDTA, ethylenediaminetetraacetic acid; EWI-F/2, Glu-Trp-Ile (EWI) motif-containing proteins; MFI, mean fluorescence intensity; minpts, minimal number of detected molecules in a cluster; Nb, nanobody; PBL, peripheral blood lymphocytes; PFA, paraformaldehyde; ROI, region of interest; SEC, size-exclusion chromatography; TCEP, Tris(2-carboxyethyl) phosphine hydrochloride; TEM, tetraspanin-enriched microdomains; TMB, 3,3',5,5'-tetramethylbenzidine; WT, wild-type; zDHHC, zinc-finger Asp-His-His-Cys domain-containing protein.

Introduction

Protein lipidation is a post-translational modification that occurs on many membrane proteins in eukaryotic cells and affects multiple biological pathways, such as membrane trafficking, protein secretion, and signal transduction [1–5]. The most studied protein lipidation form is S-acylation, which concerns a reversible attachment of a fatty acid chain to a cysteine residue via a thioester linkage. The human genome encodes 23 zinc-finger Asp-His-His-Cys domain-containing (zDHHC) enzymes, which reside predominantly in the Golgi complex and are responsible for protein acylation [6]. The most prevalent substrate for the zDHHC enzymes is palmitoyl-CoA, and residues targeted for lipidation have been described for several proteins [1]. However, attachment of acyl chains of different lengths is also observed and depends on the substrate specificity of individual zDHHC proteins [7,8], which is determined by their substrate-binding hydrophobic cavity [9]. Lipidation of membrane proteins facilitates compartmentalization in cholesterol- and sphingolipid-rich membrane domains [10,11] and can affect changes in protein conformation [12]. Membrane protein lipidation, occurring in proximity to the membrane inner leaflet or within the transmembrane domain, has been proposed to tilt transmembrane helices, influencing the protein state and orientation [3,12–14].

Tetraspanins belong to a superfamily of 33 proteins in humans with four transmembrane α -helices that are heavily lipidated on cytoplasmic membrane-proximal cysteines. Tetraspanins support the formation of an extensive functional protein network in the plasma membrane and allow spatial distribution *in cis* of specific protein partners influencing cell morphology, signal transduction, cell–cell communication, and cell migration events [15,16]. In the plasma membrane, tetraspanins form dynamic and diffuse clusters up to ca. 120 nm in size, named tetraspanin-enriched microdomains (TEMs), which are estimated to contain approximately 10 single-type tetraspanin molecules [17]. Different protein–protein and protein–lipid interactions have been proposed to support the formation of TEMs, and lipidation plays an important role [18,19]. Tetraspanin interactions are influenced by palmitoylation and involved in the formation of homodimers, heterodimers, and the association of tetraspanins with protein partners [20], including integrins, Ig-superfamily proteins, immune receptors, and metalloproteases [15,20,21].

The presence of palmitoylation has been confirmed for tetraspanins CD9 [22], CD81 [23,24], CD151 [21,25], and CD82 [26], and has been associated with

possible tetraspanin-mediated cellular functions. Importantly, CD81 palmitoylation regulates the interaction of the B-cell receptor with the CD19/CD21/CD81 complex [27], the interaction of CD81 with the serine–threonine-binding epsilon isoform of 14-3-3 protein [28], and promotes hepatitis C virus entry [29]. The absence of palmitoylation in CD151 showed diminished interaction with integrins, altered cellular distribution, and morphology [21,25]. Palmitoylation of CD82 is important for inhibition of invasiveness [30] and for the membrane organization of protein kinase C and $\alpha 4$ integrin [31,32].

Tetraspanin CD81 is expressed in different tissues including brain, muscles, and lymphoid organs and has well-established roles in B and T cells [33], as well as in the mobility of tumor and immune cells [34]. It has striking effects on the aging of mice when knocked out with its closest homologue CD9 [36]. CD81 is the only full-length tetraspanin whose structure has been solved [35]. CD9 is a widely expressed tetraspanin acting in several cellular functions such as cell migration and invasion [37,38], adhesion [39], fertilization [40,41], and muscle-cell fusion [42,43]. CD9 regulates the cell-surface assembly of numerous protein partners [39], including the Ig-superfamily EWI motif-containing single-pass membrane proteins (EWI-F and EWI-2), which have been shown to directly bind CD9 [44–46]. Although crystallization of a mutated version of CD9 has been reported, no crystal structure has been published to date [47]. CD9 features six membrane-proximal cysteines (residues 9, 78, 79, 87, 218, and 219) that undergo lipidation [48] mediated by zDHHC2 [49] and possibly other zDHHC enzymes. Previous studies using cysteine cross-linking [50] and monoclonal antibody C9BB [51] suggested that CD9 palmitoylation influences the clustering of CD9 into (homo-)oligomers, while the absence of palmitoylation increases the formation of oligomeric complexes with the protein partner EWI-2. However, how palmitoylation of specific cysteines of CD9 affects the size of TEMs, their composition, and behavior is unclear.

In this work, we investigated the site-specific lipidation of tetraspanins CD9 and CD81 as prototypes of heavily lipidated membrane proteins. We profiled their lipidation states using high-resolution native mass spectrometry (MS) [52,53]. The achieved mass-resolving power allowed us to distinguish and monitor lipidation states of CD9 and CD81. Next, we considered generation of CD9 constructs mimicking different lipidation states. Typically, membrane-proximal cysteines are mutated into alanines or serines to create nonlipidated versions of the wild-type proteins [48,50,51]. However, no amino-acid residue equivalent to an acyl

chains exists. Even though it is impossible to mimic an acyl chain by an amino-acid substitution, a putative conformational effect on the membrane protein may be mimicked by substitution with a bulky hydrophobic side chain instead of an alanine or serine residue, as done typically. To this end, we used tryptophan mutations, because they occur frequently at the lipid–water interface regions [54–56]. We analyzed these tryptophan mutants of CD9 with respect to their cellular distribution, clustering at the cell membrane and association with the direct protein partners EWI-2 and EWI-F. Our work indicates that CD9 lipidation does not influence the TEM cluster size but affects the association with protein partners. We conclude that tryptophan substitutions represent a novel strategy to study site-specific effects of lipidations in tetraspanins.

Results

Native MS profiling of lipidation in wild-type CD9 and CD81

Wild-type tetraspanins CD9 and CD81 were expressed in human cells (HEK-293) and purified using C-terminal 3Strep-tag (Fig. 1A). CD9 was solubilized and isolated with a high yield ($16 \pm 2 \mu\text{g}$ per 12 mL of cell culture) and eluted largely as a single peak in analytical size-exclusion chromatography (SEC). CD81 was expressed at variable yields (from 3 to $16 \mu\text{g}$ per 12 mL of cell culture), and its analytical SEC analysis indicated a nonhomogeneous protein distribution.

To determine the extent of lipidation, we recorded high-resolution native mass spectra of solubilized and purified wild-type CD9 and CD81, making use of Orbitrap with extended mass range [57] (Fig. S1B). The spectra revealed low-abundant peaks that matched the expected masses of the bare protein, both with and without the initial methionine (CD9 and CD81 protein sequences and expected masses are shown in Table S1). The relatively low intensity of these peaks indicated that the majority of the CD9 proteins carried modifications. We observed sets of peaks separated by 238 Da mass differences, indicating the sequential addition of one up to six palmitoyl chains. Additional peaks at higher masses, prominently visible for highly modified proteins with larger mass, can be attributed to modifications with one or more acyl chains that differ from palmitates. The relative mass difference of +28 Da, from the peaks of the purely palmitoylated species, suggested that these modifications concerned predominantly the attachment of a stearic acid chain, which has not been reported before for tetraspanins. The distributions of lipidated,

either palmitoylated or stearylated, species for CD9 and CD81 are shown in Fig. 1C, whereby we used the ion abundances in the mass spectra as proxy for the intensities. Although we observed that CD9 migrated as two bands on SDS/PAGE, we excluded the possible presence of glycans on CD9 [58,59], as such species was not detected via high-resolution native MS. The occurrence of a double band on SDS/PAGE for CD9 in both nonreducing and reducing conditions (Fig. 1A) is in line with previous studies [49,50]. Both bands of CD9 corresponded to the mass of full-length CD9 in the native MS spectra. The only other detectable modification by native MS, beside lipidation, was the removal of the N-terminal methionine. The same modifications have also been observed for CD81, which migrated as a single band on the SDS/PAGE. The majority of CD9 molecules had three or more acyl chains attached, while the most prevalent CD9 species carried five acyl chains. Instead, CD81 molecules were mostly modified by four or more acyl chains and showed increasing occurrences with higher number of acyl chains attached, with the most prevalent CD81 species carrying six acyl chains.

CD9 and CD81 present high or variable lipidation at specific sites

We analyzed the propensities of lipidation at the six membrane-proximal cysteines in CD9 and CD81 (residues 9, 78, 79, 87, 218, and 219 and residues 6, 9, 80, 89, 227, and 228, respectively) by mutating all cysteines, except one, to alanines. These alanine mutants with single cysteine lipidation sites were expressed in HEK-293 cells, solubilized, and purified; their lipidation was also profiled using high-resolution native MS (Fig. 2A,B). The expected masses of CD9 and CD81 alanine mutants are shown in Table S2. Native mass spectra of these variants showed peaks, corresponding either to no acylation, palmitoylation, or stearylation at the single cysteine sites [Fig. S2 (I–A,B)]. Palmitoylation was the most predominant lipidation for most sites on CD9 and CD81, except for cysteine 228 in CD81 that displayed ca. 50–50% palmitoylation and stearylation.

The six membrane-proximal cysteines in the CD81 crystal structure [35] represent a mixed state, due to mutations of Cys6, Cys9, Cys227, and Cys228 to serines and alkylation with iodoacetamide of the remaining free Cys80 and Cys89. Mapping our data onto this structure showed that the least lipidated residues, Cys80 and Cys227 in CD81, identical to Cys79 and Cys218 in CD9, are positioned toward the inner cone-shaped cavity of CD81 [Fig. 2C and Fig. S2 (II)]. In

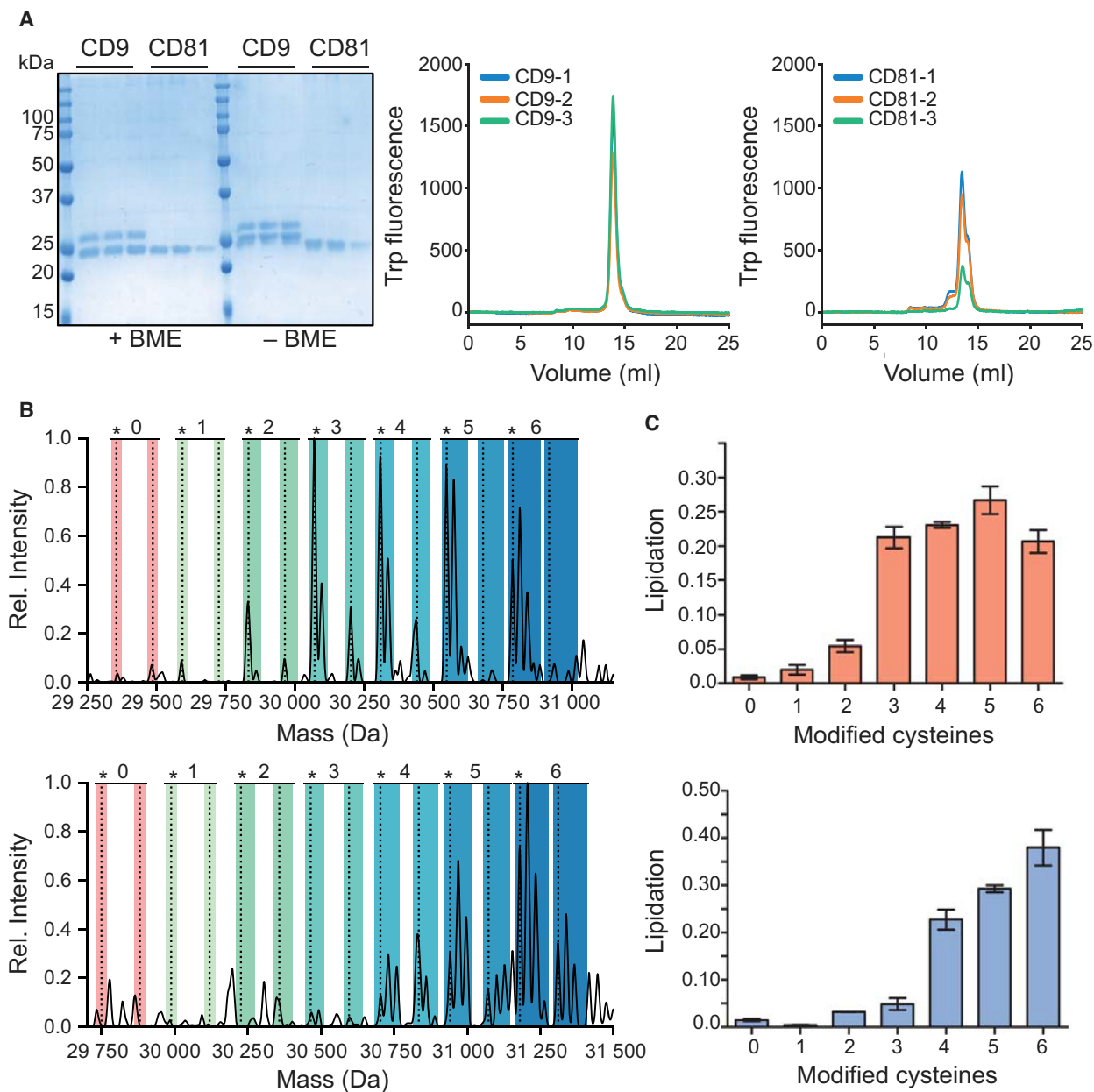


Fig. 1. Expression, purification, and high-resolution native MS analysis of CD9 and CD81 wild-type. (A) SDS/PAGE of the purified wild-type CD9 and CD81 (biological triplicate), run in reducing (+BME) or nonreducing (–BME) conditions. Analytical SEC elution profiles of the same samples. (B) Native MS spectra (deconvoluted to zero charge) of wild-type CD9 (top) and CD81 (bottom). Peaks representing the modified protein with zero to six palmitates are indicated with a dotted line at the expected position. Peaks modified with the same number of acyl chains (palmitates or stearylates) are highlighted with the same color, with their number indicated above. Peaks belonging to a proteoform with a processed N-terminal methionine are denoted with an asterisk (*) above the corresponding color bar. Two additional biological replicates can be found in Fig. S1. (C) Lipidation occurrence of wild-type CD9 (in orange) and CD81 (in blue). Intensities are derived from the integrated peaks belonging to the same color bars, therefore, including species modified with any acyl chain and in the absence or presence of the initial methionine. Bars represent the mean of three independent experiments (\pm SEM).

our previous work, we measured the palmitoylation occurrence of human Claudin-3, CD20, and two heterologous expressed bacterial membrane proteins

[52] and observed that palmitoylation displayed a stochastic distribution. Figure 2 (III) presents the predicted stochastic distributions computed from the

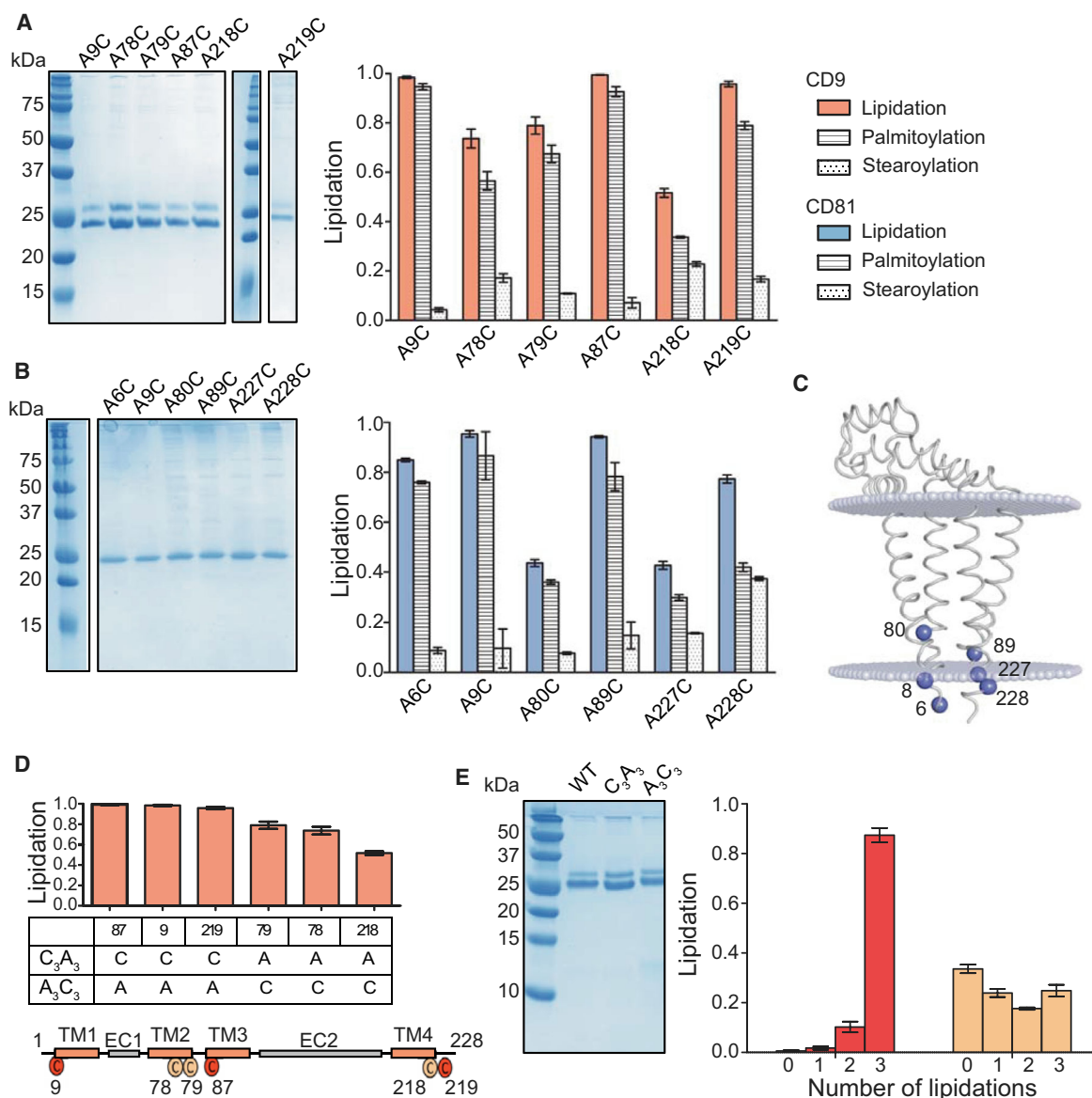


Fig. 2. Expression, purification, and high-resolution native MS analysis of CD9 and CD81 mutants with single cysteine lipidation sites and with three cysteine lipidation sites. (A) SDS/PAGE of the purified CD9 mutants with single cysteine lipidation sites and lipidation occurrence measured for each mutant (in orange). Lipidation occurrence is divided into palmitoylation (striped bars) and stearoylation (checked bars). Bars represent the mean of three independent experiments (\pm SEM). Native MS spectra can be found in Fig. S2 (I). (B) SDS/PAGE of the purified CD81 mutants with single cysteine lipidation sites and lipidation occurrence measured for each mutant (in blue). Lipidation occurrence is divided into palmitoylation (striped bars) and stearoylation (checked bars). Bars represent the mean of three independent experiments (\pm SEM). Native MS spectra can be found in Fig. S2 (I). (C) Representation of CD81 structure (PDB ID: 5TCX) where membrane-proximal cysteines are shown as blue spheres. Protein oriented with respect to the membrane planes has been retrieved from the OMP database [97]. We show a surface representation of CD81 in the same orientation in Fig. S2 (II). (D) Mean lipidation occurrence of CD9 mutants with single cysteine lipidation sites ranked in decreasing order, showing the frequently modified cysteines (Cys9, Cys87, and Cys219), followed by the moderately lipidated cysteines (Cys79, Cys78, and Cys218). Below the bar chart, a scheme of CD9 mutants with three cysteine lipidation sites (denoted C_3A_3 and A_3C_3 , based on the ranking order) and the CD9 sequence displaying the location of the Cys triplets, frequently modified (in red) or moderately modified (in orange). A comparison between the measured lipidation occurrence and the occurrence predicted from a stochastic distributions model based on the lipidation propensities of single cysteine sites for CD9 and CD81 can be found in Fig. S2 (III). (E) SDS/PAGE, showing the purified mutants and, for comparison, wild-type CD9. Mean lipidation occurrence of C_3A_3 (in red) and A_3C_3 (in orange) was measured in three independent experiments (\pm SEM). A sequence alignment of the 33 human tetraspanins, a scheme containing the initial set of lipidation mutants, and their initial expression are depicted in Fig. S2 (IV).

lipidation propensities of single cysteine sites for CD9 and CD81. The correlations between observed and predicted distributions were $c = 0.65$ and $R^2 = 0.41$, respectively (cf. $R^2 > 0.9$ found for Claudin-3 and CD20 [52]), indicating a more intricate process than mere stochastic lipidation as observed for Claudin-3 and CD20.

Use of tryptophan to mimic lipidation in CD9

We grouped the membrane-proximal cysteines of CD9 based on their lipidation propensities into three most frequently lipidated residues 87, 9, and 219, and the three less frequently or moderately lipidated residues 79, 78, and 218 (Fig. 2D). Native MS profiling of a CD9 variant with cysteines at the three most frequently lipidated sites and alanines at moderately lipidated sites (denoted C₃A₃; Fig. 2E) yielded predominantly (~85%) triple-lipidated CD9, while a variant with three alanines and three cysteines, at the other sites (denoted A₃C₃), yielded a mixture of non-, single-, double-, and triple-lipidated species [Fig. 2E and Fig. S2 (I-C)]. The expected masses of CD9 mutants with three cysteine lipidation sites are listed in Table S2. These observations reflect those made for wild-type CD9, showing that three sites are typically lipidated in CD9 yielding species with three up to six attached acyl chains.

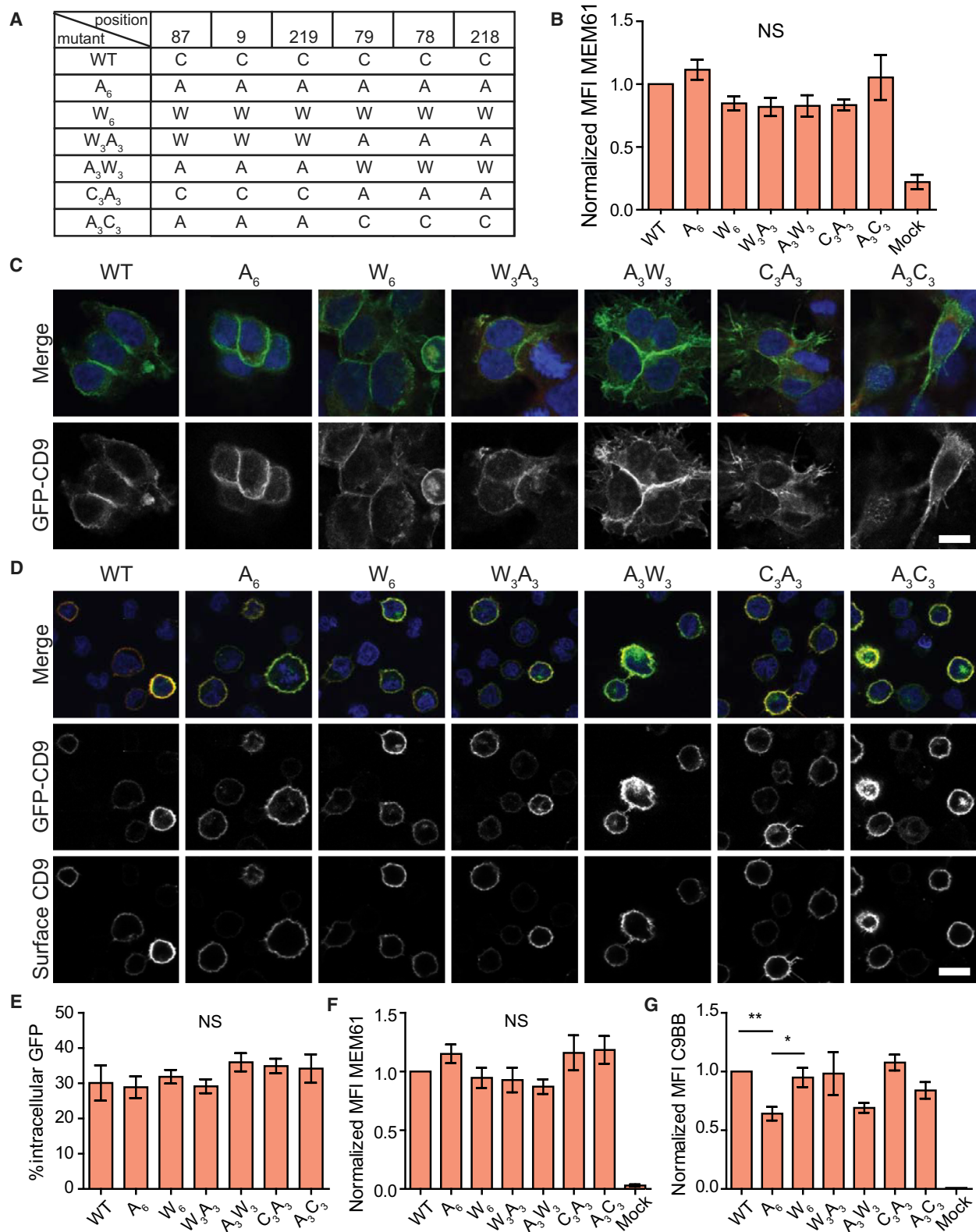
A set of CD9 mutants was designed as a 3Strep-GFP fusion, to initially monitor their expression in HEK-293 cells, purification, and stability [mutants are listed in Fig. S2 (IV-B)]. We substituted the most frequently lipidated cysteines (residues 9, 87, 219) with bulky aromatic (Trp) residues, while the remaining three cysteines were mutated to alanines, denoted W₃A₃. Conversely, we generated mutants where we

substituted the moderately lipidated cysteines (residues 78, 79, 218) with aromatic residues, while the three other cysteines were mutated to alanines (A₃W₃). Similarly, we created two nonlipidated versions of CD9, in which the six cysteines were mutated to alanine (A₆) or to serine (S₆), in line with previously reported mutants [48,50,51], and a version of CD9, where we mutated all cysteines to tryptophans (W₆). GFP fluorescence-assisted SEC traces of the CD9 3Strep-GFP-tagged constructs showed a symmetrical peak, indicating that the proteins are monodisperse and folded [Fig. S2 (IV-C)]. However, CD9 S₆ did not elute as a monodisperse peak, indicating heterogeneous forms. CD9 A₆ was therefore chosen over CD9 S₆ to represent the nonlipidated state. The final set of mutations used to mimic lipidation states in functional cellular studies is listed in Fig. 3A.

Lipidation does not affect surface expression or trafficking of CD9

Because most CD9 functions are carried out at the plasma membrane, we first tested whether all mutants were expressed on the cell surface to similar extents. We overexpressed the different GFP-tagged CD9 constructs in HEK-293 cells, stained for surface CD9 using the antibody MEM61, and measured the mean fluorescence intensity (MFI) by flow cytometry (Fig. 3B). Surface expression of the nonlipidated mutant CD9 A₆ was similar to wild-type CD9, indicating that lipidation is not involved in the transport of CD9 to the plasma membrane, which is in line with previous reports [49]. Since the other CD9 mutants showed similar CD9 surface expression and microscopy experiments showed a comparable intracellular distribution of GFP signal (Fig. 3C), we exclude major

Fig. 3. Lipidation does not affect surface expression or trafficking of CD9 but affects CD9 complexes in a site-specific way. (A) Overview of the lipidation mutants. (B) Comparable CD9 surface expression on HEK-293 cells transfected with GFP-tagged WT CD9 or one of its lipidation mutants as assessed by flow cytometry using the MEM61 antibody. Depicted MFI values are normalized to WT CD9 and represent the mean of 3–7 independent experiments (\pm SEM). (C) Similar cellular localization of WT CD9 and its lipidation mutants in HEK-293 cells as shown by confocal microscopy. CD9 is visualized with a GFP-tag (green), and the nucleus is stained with DAPI (blue). (Scale bar = 10 μ m). (D) Confocal microscopy shows the localization of the total pool of CD9 (visualized by its GFP-tag, shown in green), and of the membrane-exposed pool of CD9 (visualized by MEM61 antibody staining, shown in red) in RAJI cells overexpressing WT CD9 or its lipidation mutants. The merged channel also shows the nucleus stained by DAPI in blue (Scale bar = 10 μ m). (E) The proportion of intracellular WT CD9 molecules is similar to the proportion of the different lipidation mutants. This proportion is calculated by dividing the fraction of GFP signal not overlapping with the membrane staining by the total GFP signal. Depicted values show the mean (\pm SEM) of 3 independent experiments, 10 cells per experiment. (F) Flow cytometry shows a comparable CD9 surface expression on RAJI cells transfected with GFP-tagged WT CD9 or one of its lipidation mutants as assessed by flow cytometry using the MEM61 antibody. Depicted values are normalized to WT CD9 and represent the mean of 6–11 independent experiments (\pm SEM). (G) Differential binding of conformation-dependent antibody C9BB to WT CD9 and the different lipidation mutants (the same samples as depicted in pane F) was measured by flow cytometry. Depicted values are normalized to WT CD9 and represent the mean of 3–8 independent experiments (\pm SEM). Significance was calculated by using a Friedman test followed by Dunn's multiple comparison testing. * $P \leq 0.05$ and ** $P \leq 0.01$.



folding or trafficking defects as a result of the introduced mutations.

To rule out the possibility that endogenously expressed CD9 in HEK-293 cells would mask potential trafficking defects, the experiments were repeated in the CD9-negative B-cell line RAJI. Both the intracellular localization (Fig. 3D) and the percentage of GFP signal that is intracellular, that is, not overlapping with surface CD9 staining (Fig. 3E), were comparable for the different GFP-tagged CD9 constructs in RAJI cells. These observations, together with a similar CD9 surface expression (Fig. 3F), confirmed that lipidation of CD9 does not affect its trafficking or surface expression.

Effects of site-specific lipidation mimicked by tryptophan mutations

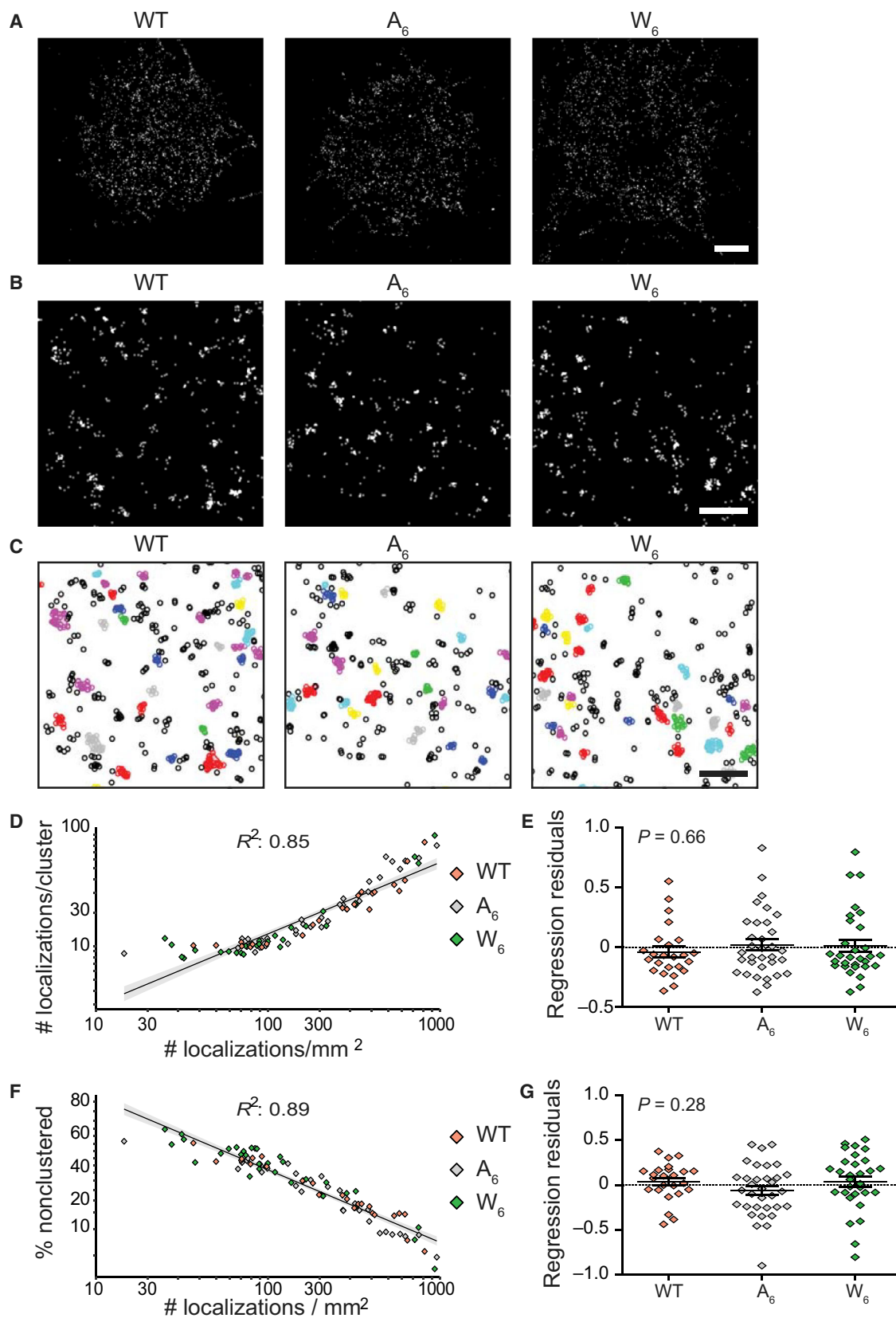
Although total surface expression of CD9 was unaffected by the introduced mutations, CD9 protein complexes formed at the cell surface could be altered. To test this, we used the antibody C9BB, of which the binding has been reported to be influenced by the composition of the CD9 complexes [51]. C9BB preferentially binds homoclustered CD9 and its binding is strengthened by both lipidation and expression of integrins, while the absence of lipidation and association with the protein partner EWI-2 diminished C9BB staining [51]. Although the surface expression of the different CD9 constructs in RAJI cells was found to be similar (Fig. 3E,F), C9BB staining of the same samples showed marked differences (Fig. 3G). In agreement with Yang *et al.*, we detected a significant decrease in C9BB binding to CD9 A₆ mutant compared with binding to wild-type CD9. Interestingly, the CD9 W₆ mutant showed similar levels of C9BB

binding to the wild-type protein. Furthermore, we observed differential C9BB binding when the cysteines were replaced by sets of tryptophans and alanines, W₃A₃ and A₃W₃ (Fig. 2D). Binding of C9BB to CD9 W₃A₃ was comparable to the wild-type, whereas CD9 A₃W₃ was more comparable to nonlipidated CD9 A₆ (Fig. 3G). We observed that C9BB binds to similar extent to CD9 W₃A₃ and C₃A₃ mutants. Also, CD9 A₃W₃ and A₃C₃ mutants showed similar levels of C9BB binding, but lower, though not significant, than for the complementary mutant W₃A₃ (or C₃A₃). Because C9BB stained to similar extent complementary mutants, these results are in line with a site-specific effect of lipidation on CD9 complexes.

Generation of anti-CD9 nanobody probe for super-resolution microscopy

Next, we generated a novel nanobody (Nb)-based anti-CD9 fluorescent probe to study the spatial organization of CD9 on membranes at single-molecule resolution by super-resolution microscopy [60]. After immunization of llamas with purified A₆ mutant CD9, we constructed a phage display nanobody library with a size of 1.1×10^8 . Phage display on C-terminal 3Strep-tagged wild-type CD9 yielded several Nb clones that specifically bound CD9 [Fig. S3 (I-A,B)]. For the purpose of the current study, we selected Nb clone 4C8, as it displayed the highest binding affinity on purified wild-type CD9 (K_D of 0.6 nM) and on HeLa cells (K_D = 0.9 nM) [Fig. S3 (I-A,B)]. Binding of 4C8 Nb to adherent cells indicated that its epitope was located in the extracellular loops of CD9 [Fig. S3 (I-B)]. We purified the C-terminal Cys-EPEA-tagged Nb 4C8 from the periplasmic fraction of *Escherichia coli* cells and site directly conjugated it to maleimide-Alexa

Fig. 4. Lipidation of CD9 does not affect its clustering on the cell surface. (A) Reconstructed dSTORM images of representative RAJI cells overexpressing WT, A₆, or W₆ versions of CD9 stained with an Alexa 647-conjugated anti-human CD9 nanobody. Scale bar is 2 μm. A characterization of the CD9 nanobody can be found in Fig. S3 (I). (B) Zoom-in of the cells depicted in A. Scale bar is 0.5 μm. (C) Convex Hull representation of the zoomed images shown in (B) generated with the DBSCAN algorithm using an ε of 50 nm and a minpts of 5. Localizations that are classified as part of a cluster are depicted as circles in the same color, and localizations that are classified as nonclustered appear as black circles. Scale bar is 0.5 μm. Figure S3 (II) shows that different ε and minpts values do not induce differences between samples. (D) Quantification of the number of localizations per cluster as calculated by DBSCAN versus the density of localizations per square μm cell surface. Each dot in the graph represents the mean of all clusters in a single cell. The regression curve, R^2 , and 95% confidence interval are derived from a linear regression model of log # localizations per cluster versus log localizations per μm² on the pooled data of all mutants. $N = 3$ independent experiments, $n > 30$ cells per CD9 construct. (E) Residuals of the regression model for the different CD9 constructs and a P -value as calculated by ANOVA analysis. Each dot represents a single cell, and the mean of all cells is depicted ± SEM. (F) Quantification of the percentage of localizations in a cell that was classified by DBSCAN as nonclustered versus the density of localizations per square μm cell surface. Each dot in the graph represents a single cell. The regression curve, R^2 , and 95% confidence interval are derived from a linear regression model of logit % nonclustered localizations versus log localizations per μm² on the pooled data of all mutants. $N = 3$ independent experiments, $n > 30$ cells per construct. (G) Residuals of the regression model for the different CD9 constructs and a P -value as calculated by ANOVA analysis. Each dot represents a single cell, and the mean of all cells is depicted ± SEM.



647, via the introduced free C-terminal cysteine [Fig. S3 (I-C)]. The final probe had a degree of conjugation of 50% and contained less than 10% of free dye. Finally, its binding affinity was validated on purified wild-type CD9, yielding a K_D of 3.1 nM [Fig. S3 (I-D)].

CD9 nanoscale clustering on the cell surface is not affected by lipidation

Wild-type CD9 and its A_6 and W_6 mutants were overexpressed in CD9-negative RAJI cells, stained with the Alexa 647-conjugated 4C8 nanobody, and the basal membrane of aldehyde-fixed cells was imaged using a dSTORM setup. Whole-cell dSTORM showed the nanoscale organization of CD9 on the cell surface (Fig. 4A), whereas individual molecules can be observed in the magnified images (Fig. 4B). The latter images showed a population of wild-type, A_6 , and W_6 CD9 molecules, which appeared clustered in small groups, and a second population of single CD9 molecules that did not associate in clusters.

To compare the clustering of different CD9 lipidation mutants, we applied the density-based spatial clustering (DBSCAN) algorithm [61]. Given a distance range (ϵ) and a minimal number of detected molecules in a cluster (minpts), this algorithm assigns each detected molecule to a specific cluster or it assigns it as nonclustered. In the convex Hull representation of the magnified images generated with DBSCAN (Fig. 4C), localizations (detection events of single molecules) that are classified as part of a cluster are depicted as circles in the same color and localizations that are classified as nonclustered appear as black circles. Based on previously reported tetraspanin-cluster diameter and density [17,32], an ϵ of 50 nm and a minpts of 5 were chosen for quantification. However, similar conclusions were obtained using different ϵ and minpts values [Fig. S3 (II-A,B)]. The number of localizations in a cluster showed a strong correlation with the density of molecules at the cell surface for all the three tested CD9 mutants (Fig. 4D). The regression curve in this figure is derived from a linear regression model of $\log \#$ localizations per cluster versus \log localizations $\cdot \mu\text{m}^{-2}$ on the pooled data of all mutants. This regression model was used to check whether lipidation affects the number of molecules per cluster independently of density. Since the residuals of this regression are not significantly different between the different CD9 constructs (Fig. 4E), these data do not provide evidence for an effect of lipidation on the number of molecules per cluster. Similarly, the fraction of localizations that is not assigned to a cluster was strongly

dependent on the CD9 expression level on the cell surface (Fig. 4F). The regression curve in this figure is derived from a linear regression model of \log % non-clustered localizations versus \log localizations $\cdot \mu\text{m}^{-2}$ on the pooled data of all mutants. Again, the residuals of this regression model do not provide evidence for an effect of lipidation on the fraction of molecules that is not assigned to a cluster (Fig. 4G). In conclusion, we found no evidence that lipidation, alanine nor tryptophan mutations, directly affected either the number of molecules per cluster or the fraction of nonclustered molecules.

Site-specific effects on binding direct protein partners mimicked by tryptophan mutations

Whereas the spatial organization of CD9 on the cell surface was unaffected, the observed differences in the binding of C9BB to the CD9 mutants (Fig. 3G) may be the result of a different composition of the CD9 complexes. Therefore, we analyzed the association of CD9 variants with the direct protein partners EWI-F and EWI-2 by overexpressing C-terminal 3Strep-tagged CD9 with either EWI-F or EWI-2 in HEK-293 cells. Because complexes of CD9 with either EWI-F or EWI-2 are maintained in relatively stringent detergents (i.e., Brij96, digitonin, and Triton X-100) [44-46], we employed n-dodecyl- β -D-maltopyranoside for solubilization and co-purification of 3Strep-tagged CD9, as we did for the initial MS characterization of purified protein. When the CD9 mutants were expressed in HEK293 cells, endogenous EWI-F and, to a lesser extent, EWI-2 was co-purified with CD9 indicating stable complex formation with wild-type CD9, as described previously [44-46] (Fig. 5A). Interestingly, endogenous EWI-F was also co-purified with CD9 mutants C_3A_3 and W_6 , while this was not the case for the other CD9 mutants. To further assess the interaction between the CD9 mutants and EWI-2 and EWI-F, the co-purification experiments were repeated in HEK293 cells co-expressing EWI-F or EWI-2 (Fig. 5B,C). In these cells, hardly any EWI-F or EWI-2 was found associated with the nonlipidated CD9- A_6 variant (Fig. 5B,C). The experiments showed weak-to-very weak association of EWI-2 with the tryptophan and alanine variants of CD9 (Fig. 5C). Instead, EWI-F was co-purified efficiently with C_3A_3 , followed by W_6 and, to a lesser extent, with W_3A_3 , while only weak EWI-F association was observed when using CD9 A_3C_3 and its counterpart A_3W_3 . Since EWI-F colocalized to a similar extent with the different CD9 variants, we can exclude that the observed differences are caused by aberrant expression or localization of

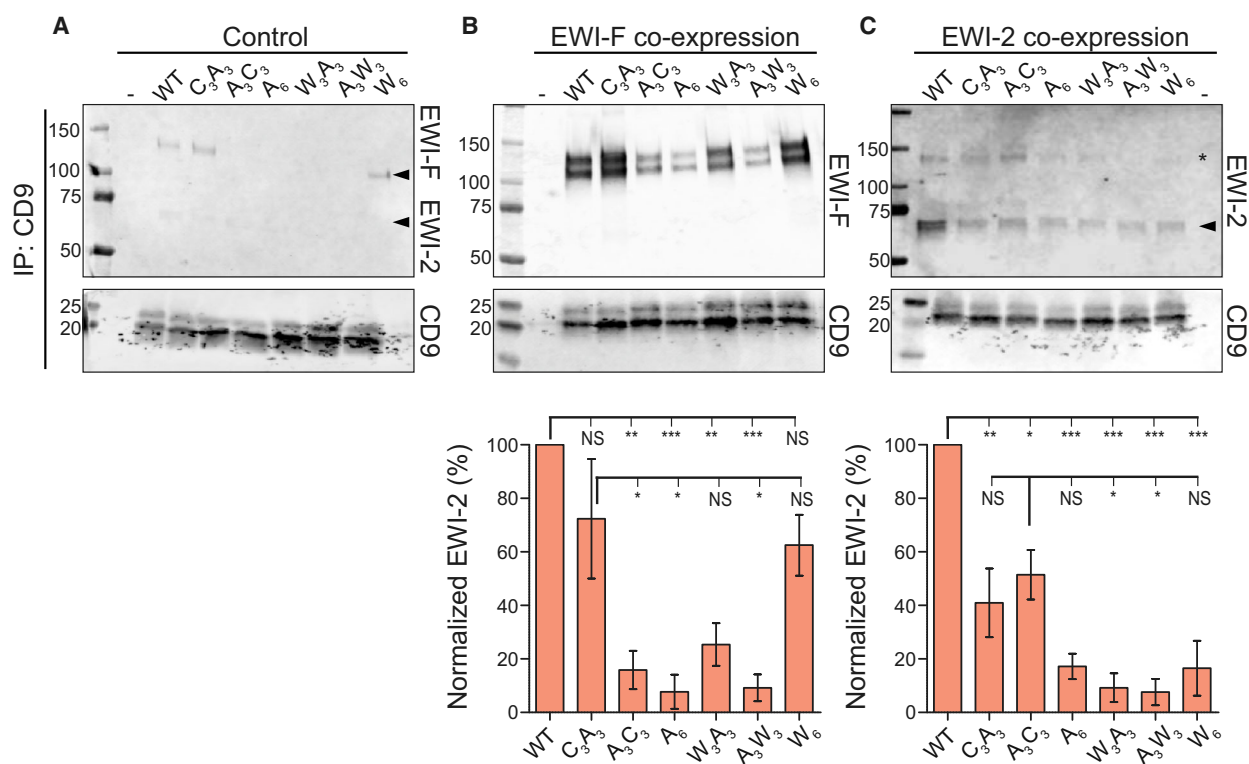


Fig. 5. Site-specific lipidation effects on the interaction of CD9 with EWI-F and EWI-2. (A) Purified Strep-tagged CD9 wild-type and CD9 lipidation mutants (C₃A₃, A₃C₃, A₆, W₃A₃, A₃W₃, and W₆) were visualized by western blotting. hEWI-F and hEWI-2 antibodies were used in the upper panel. hCD9 antibody was used in the lower panel. Faint bands corresponding to endogenous EWI-F and EWI-2, co-purified with the CD9 mutants, are marked with an arrowhead. (B) Co-purification of Strep-tagged CD9 WT and CD9 lipidation mutants with EWI-F. CD9 mutants W₆ and C₃A₃ were preferentially co-purified with EWI-F, while mutant W₃A₃ was moderately associated with EWI-F. CD9 mutants A₃C₃, A₃W₃, and A₆ bound instead EWI-F to a lower extent. Bar chart displays the quantification of EWI-F signal intensities divided by the signal of the captured CD9 (mean ± SEM, *n* = 3). The mean for CD9 wild-type co-purified with EWI-F was set to 100%. Significance was calculated by using one-way ANOVA and Bonferroni's multiple comparison testing. **P* ≤ 0.05, ***P* ≤ 0.01, and ****P* ≤ 0.001. Figure S4 shows that the observed differences in CD9 - EWI-F co-purification are not due to CD9 and EWI-F aberrant colocalization. (C) Co-purification of the same CD9 mutants with EWI-2 shows no preferential binding to CD9 site-specific lipidation mutants, although more EWI-2 was associated with CD9 wild-type. Lower panel displays the quantification of EWI-2 signal intensities divided by the signal of the captured CD9 (mean ± SEM, *n* = 3). The mean for CD9 wild-type co-purified with EWI-2 was set to 100%. Significance was calculated by using one-way ANOVA and Bonferroni's multiple comparison testing. **P* ≤ 0.05, ***P* ≤ 0.01, and ****P* ≤ 0.001. The band representing EWI-2 is marked with an arrowhead, and an additional minor band below 150 kDa (the molecular mass of EWI-2 corresponds to 65 kDa), possibly representing an EWI-2 dimer, is marked with *.

one of the proteins (Fig. S4A,B). We therefore conclude that, while the effect of CD9 lipidation does not seem to have a site-specific component in its interaction with EWI-2, the interaction with EWI-F shows a clear dependency on the lipidation of a specific set of cysteines.

Discussion

CD9 is a prototypical membrane protein with multiple membrane-proximal cysteines. In this work, we profiled CD9 lipidation and revealed different propensities for lipidation by either palmitoyl or stearoyl chains

that indicated that both CD9 and its close homologue CD81 are nonstochastically lipidated. Furthermore, we addressed the dependency of CD9 binding to EWI-F and EWI-2 on site-specific lipidations, using CD9 variants in which either the three most or the three least frequently lipidated cysteine residues are maintained for lipidation (CD9-C₃A₃ and CD9-A₃C₃, respectively). We substituted cysteines by alanines to block lipidation, instead of serines [51], because of reduced protein stability of CD9-S₆ [Fig. S2 (IV-C)]. Our findings indicate that site-specific lipidations of CD9 influence the behavior of the tetraspanin clusters which, despite maintaining the same number of molecules, are

composed of different protein partners. We used tryptophan mimicry to induce a putative conformational arrangement in the tetraspanin, mimicking the effect determined by the attachment of acyl chains at specific sites. Substitution of tryptophan to membrane-proximal cysteines in CD9 had different effects. Firstly, tryptophan partially rescued the effect of CD9 lipidation for binding of EWI-F, since mutants CD9-W₆ and, albeit to a lesser extent, CD9-W₃A₃ pulled down EWI-F as did wild-type CD9 and CD9-C₃A₃ (Fig. 5B). Secondly, tryptophan mimicry did not rescue CD9 lipidation for binding of EWI-2. To our knowledge, this is the first time that tryptophan mutations are used as a tool to test the functional effects of (site-specific) lipidation of a membrane protein, directly influencing the binding of protein partners.

Site-specific aspects of lipidation have been shown for protein targeting to the cell surface, trafficking of the ion channels AMPA, NMDA, and BK, and to interplay with other post-translational modifications [62]. Recently, S-palmitoylation of β_2 -adrenergic receptor has been shown to be site-specific and distinct in human and rodent proteins. In particular, palmitoylation of Cys153 and Cys292 within the human β 3AR increased membrane-receptor abundance, but only Cys361/363 palmitoylation enhanced membrane-receptor half-life [63]. In our work, we observed that the site-specific lipidation of CD9 did not affect protein targeting or localization at the plasma membrane, but it affected primarily CD9 interactions with other proteins. The differential interactions between EWI-F and different lipidation mutants of CD9 represent an example of function associated with site-specific lipidation in the tetraspanin protein family.

Unlike the binding of protein partners, different lipidation states of CD9 did not affect clustering of CD9 on the cell surface (Figs 3A–F and 4D,E). dSTORM microscopy revealed a similar number of CD9 molecules in nanoclusters, most likely TEMs, and a similar population of nonclustered proteins for the different lipidation mutants of CD9. The appearance of a clustered and a nonclustered population of CD9 molecules is in line with the detection of confined – and Brownian – diffusion modes of single CD9 molecules in live cells [64]. Whereas we found no evidence that lipidation did affect the number of molecules in CD9 clusters (Fig. 4D), this is not a general characteristic of tetraspanins since loss of palmitoylation was shown to reduce cluster size of tetraspanin CD82 [31]. Interestingly, we observed a strong correlation between the expression level of CD9 and its clustering behavior (Fig. 4D,E), which is in line with the observation that CD82 forms larger clusters upon overexpression [31]. Previous work has shown that

CD9 could interact with EWI-2 via two independent regions including part of the second and third transmembrane helix (residues 69–116) and the second half of CD9 large extracellular loop (after the CCG tetraspanin-consensus motif) [65]. It has also been proposed that EWI-2 interacts with CD9 via a region that excludes the two more distal N-terminal Ig domains [45]. EWI-F was reported instead to interact with CD9 via its transmembrane domain [66], while other groups have shown that a truncated form of EWI-F, corresponding to the extracellular region close to the transmembrane domain (residues 724–832), co-precipitates with CD9 [67]. These studies indicate that different regions of EWI proteins are involved in CD9 binding. Also, we showed a clear difference between CD9 binding of EWI-F and EWI-2, indicating that only the three most frequently lipidated sites are required for EWI-F binding, while no specific cysteines are required for EWI-2 binding.

Mapping lipidation profiles of single cysteine variants of transmembrane proteins onto 3D structural data suggests that site-specific lipidation propensities are possibly correlated with the accessibility of the cysteine substrates for their membrane-embedded acyltransferases [52]. In particular, the positions of Cys80 and 227 are located toward the inner protein cavity in the structure of CD81 and are the least acylated sites. The lipidation profiles of CD9 and CD81 do not fit a simple stochastic model for lipidations at multiple sites, in contrast with what has been observed for Claudin-3 and CD20 [52]. Though not experimentally proven, the potential occurrence of multiple conformations of CD9 and CD81, with different cysteine-SH accessibility, will cause a nonstochastic lipidation profile. Such conformation-dependent lipidation may explain the observed enhanced palmitoylation upon antibody-induced co-ligation of CD81 [27].

Palmitoylation is the dominant form of lipidation in CD9 and CD81; however, our native mass spectrometry experiments also revealed a population of these tetraspanins modified with stearic acid. Interestingly, despite the low abundance, stearic acid modifications show a variable and site-specific occurrence and were not detected in other membrane proteins, analyzed with the same high-resolution methodology [52]. In addition, the presence of different acyl substrates could possibly contribute to the nonstochastic lipidation profile, displayed by CD9 and CD81. Although blood platelet proteins have been reported to be stearylated [68] and CD9 is highly abundant membrane protein in platelets [69], this modification has never been described before for tetraspanins. Stearoylation has been reported for a limited number of other proteins [2], including influenza glycoproteins [70], P-selectin

[71], and the transferrin receptor [72]. It remains to be studied whether stearoylation of tetraspanins has a specific functional role.

The process of S-acylation is regulated by 23 different zDHHC enzymes [73] and, in HEK-293 cells, the expression of 20 of these enzymes has been detected [74]. Removal of S-acylation is performed by acylthioesterases [75], namely APT1/2 [76,77] and the ABHD17 protein family [78], making acylation a reversible modification. We hypothesize that CD9 function may also be regulated by selective (de-) S-acylation of specific cysteines. In principle, this regulation could happen right after protein synthesis or later at the cell membrane, since the major palmitoylating enzyme of CD9, zDHHC2, is found in both compartments [49,79]. However, although zDHHC enzymes are known to be specific for certain target proteins, it is unclear whether they can also be specific for specific cysteine residues [62]. In that respect, it is interesting to note that the ratio between the occurrence of palmitoylation and stearoylation shows site-specific differences (Fig. 2A,B). This suggests that lipidation of tetraspanin CD9 and CD81 is governed by different zDHHC enzymes with a specificity for specific cysteines. Furthermore, a de-acylation enzyme for CD9 is still to be discovered. Extensive and careful analysis of CD9 lipidation in different conditions will be required to prove the hypothesis of CD9 regulation by selective (de-)acylation of specific cysteines.

Amino-acid substitutions that mimic post-translational modifications, in particular substitution of a serine to an aspartate or glutamate, have proven to be a useful tool to study phosphorylation of specific residues in a range of proteins, such as tau [80,81], Sox2 [82], α 4-integrin [83], VASP [84], and tropomyosin [85]. The tryptophan mimicry used in this work may represent a similar powerful strategy, based on sequence mutagenesis, which allows the protein to switch into a determined and nonreversible conformational state. We showed that the lipidation mutants used in this work mimic their lipidated constructs counterparts, as comparable outcomes were obtained for W_6 and wild-type CD9, for W_3A_3 and C_3A_3 , and for A_3W_3 and A_3C_3 , in binding to C9BB antibody. Similarly, wild-type CD9 and variants W_6 and W_3A_3 showed enhanced binding to the protein partner EWI-F.

In conclusion, our findings reveal that specific lipidation sites on membrane proteins have specific functions. We anticipate that the use of tryptophan mimicry to study site-specific membrane-protein lipidation has important implications to decipher protein lipidation-associated functions, surface distribution, and possible conformational states in other systems.

Materials and methods

DNA constructs and overexpression

The cDNA encoding human CD9 and CD81 was purchased from GeneArt in a pJ201 plasmid. The cDNAs encoding human EWI-F and EWI-2 were obtained from Source BioScience in a pENTR223.1 and pCMV-SPORT6 plasmids, respectively. For expression in HEK-293 cells, CD9 and CD81 were subcloned in an expression vector containing a start codon and a C-terminal triple repeat Strep II tag followed by a stop codon (U-Protein Express B.V., Utrecht, the Netherlands) using a 5' BamHI and 3' NotI restriction sites. EWI-F and EWI-2 were subcloned in an expression vector containing a cystatin secretion signal peptide, a start and a stop codon (U-Protein Express B.V., the Netherlands) using a 5' BamHI-compatible BsmBI (for EWI-F) or BglII (for EWI-2) and 3' NotI restriction site. For initial expression, trials of the lipidation mutants CD9 were subcloned in an expression vector containing an N-terminal 3Strep-GFP-tag (U-Protein Express B.V., the Netherlands). For large-scale production and nanobody generation, the CD9 A_6 mutant was subcloned in an expression vector having a C-terminal His₆ fused to an EPEA tag (U-Protein Express B.V., the Netherlands).

All the mutagenesis reactions were performed using the Q5 Site-Directed Mutagenesis Kit (NEB, Ipswich, MA, USA). For co-transfections, vectors containing CD9 and EWI-F/EWI-2 were mixed in 1 : 1 molar ratio. All the constructs were diluted 100-fold (w/w) with a dummy plasmid expressing the tripeptide MGS [86], which yields the highest expression for membrane proteins [52]. Constructs were then transiently expressed in 12 mL, for MS analysis, or in 25 mL, for co-purification, HEK-293-EBNA1 suspension cells (supplied by U-Protein Express B.V., the Netherlands).

The constructs used for (dSTORM) microscopy and flow cytometry experiments were obtained by a PCR reaction on the different CD9 (mutant) constructs and subcloned into an psGFP2-C1 vector [87]. First, the following primers, Fwd: AGTATTGAGAATTCAGGAATGCCGGTCAAAGGAGGC and Rev: AGTATTGAGTCGACAGTATTGACTAGAC-CATCTCGCGGTTCC, were used to add an EcoRI and a SalI restriction site to the coding sequence. Then, the resulting PCR product was ligated into a EcoRI and SalI cut psGFP2-C1 vector.

Purification of CD9, CD81, and co-purification of CD9-EWI-2 and CD9-EWI-F complexes

Cells were harvested 96 h after transfection and resuspended in 1.5 mL of Buffer A [25 mM HEPES/NaOH pH 7.5, 150 mM NaCl, 1 tablet of protease inhibitor cocktail (Roche, Basel, Switzerland), and 1% w/w *n*-dodecyl β -D-

maltopyranoside (DDM; Anatrace, Maumee, OH, USA)]. Solubilized cell extracts were separated by ultracentrifugation (100 000 *g*, 1 h, 4 °C), and 20 μ L Strep-Tactin Sepharose High-Performance beads (GE Healthcare, Chicago, IL, USA) were applied to the supernatant, supplemented with 3 mL of Buffer B (25 mM HEPES/NaOH pH 7.5, 150 mM NaCl, and 0.025% w/v DDM). After overnight incubation, beads were washed with Buffer B and purified CD9, CD81, and CD9-EWI-2 and CD9-EWI-F complexes were eluted with 2.5 mM d-desthiobiotin in 50 μ L. CD9 and CD81 sample purity and stability were assessed via Coomassie-stained 14% SDS/PAGE and using an analytical Superdex 200 10/300 increase SEC (GE Healthcare) equilibrated in Buffer B. Tryptophan fluorescence was detected via excitation at 275 nm and emission at 354 nm using an inline fluorescence detector (Shimadzu, Kyoto, Japan). For N-terminal GFP-tagged constructs, GFP fluorescence was detected using the same system via excitation at 488 nm and emission at 509 nm.

Antibodies and western blotting

For detection of CD9, a rabbit anti-hCD9 (ab7999; Abcam, Cambridge, UK) primary antibody was used. For detection of EWI-F and EWI-2, a rabbit anti-hEWI-F (SAB2700379; Sigma, Saint Louis, MO, USA) and a rabbit anti-hEWI-2 (HPA011917; Sigma) primary antibodies were used, respectively. As secondary antibody, a donkey anti-rabbit IRDye 680LT antibody (LI 926-68023; Westburg, Leusden, the Netherlands) was chosen. Western blotting was performed on three biological replicates according to standard protocols using a Trans-Blot Turbo transfer system (Bio-Rad, Hercules, CA, USA) on mini- or midi-nitrocellulose membranes (Bio-Rad). For blocking, the Odyssey blocking buffer (LI-COR, Lincoln, NE, USA) was used and images were acquired using the LI-COR Odyssey® Infrared Imager. Quantification of the western blot bands of EWI-F or EWI-2 was performed using IMAGE STUDIO LIGHT (LI-COR). The total protein signal includes the respective upper and lower bands of CD9, EWI-F, and EWI-2. For quantification, the signal of EWI-F and EWI-2 was normalized to the relative signal of CD9. Signal intensities of EWI-F and EWI-2 were plotted (mean \pm SEM) using the GRAPH PAD PRISM 7 software (GraphPad Software, San Diego, CA, USA), and the control CD9 wild-type-EWI-F/2 sample was set to 100%.

Native mass spectrometry

Purified proteins were buffer exchanged to 150 mM ammonium acetate, 0.025% (w/v) DDM, pH 7.5, using Micro Bio-Spin columns (Bio-Rad). An aliquot of 1–2 μ L was loaded into gold-coated borosilicate capillaries (prepared in-house) for nano-electrospray ionization. Samples were analyzed on either a modified Orbitrap EMR instrument

(Thermo Fisher Scientific) or a QE UHMR instrument (Thermo Fisher Scientific) [57,88–90]. Capillary voltage was set at 1400 V, source fragmentation or in-source-trapping to 50 V, and extended trapping 200–300 V. Nitrogen was used as collision gas. Spectra were acquired using an acquisition time of 32 or 64 ms per scan, averaged over several scans, typically 1 min. Recorded spectra were deconvoluted using Intact Mass software (Protein Metrics) [91], and relative lipidation levels were extracted by integrating over the manually selected mass range, including all relevant masses. Relative palmitoylation/stearoylation ratios were extracted by taking the top intensities at the expected mass. All data analysis following spectra deconvolution was performed using PYTHON 3.6 scripts (Wilmington, DE, USA).

Quantitative analysis

Predictions of wild-type lipidation patterns were calculated using a Poisson binomial distribution with each lipidation site having a unique lipidation probability. The fraction of lipidated – combined palmitoylated and stearoylated – single cysteine mutants of CD9 and CD81 was used as the lipidation propensity. Single-site propensities were obtained by averaging of biological triplicate experiments. All modeling was done using PYTHON 3.6 scripts.

Cell culture and transfection

RAJI B cells were cultured in RPMI 1640 medium supplemented with 10% FBS (Greiner Bio-One, Alphen aan den Rijn, The Netherlands), 1% ultraglutamine (Lonza, Basel, Switzerland), and 1% w/v antibiotic–antimycotic. Transient transfections were performed in the absence of antibiotic–antimycotic using the SF Cell Line 4D-Nucleofector X Kit and 4D Nucleofector System (Lonza). For protein purification, HEK-293 cells were cultured in Freestyle 293-Expression medium (Invitrogen Gibco) supplemented with 0.02% FBS (Invitrogen Gibco, Waltham, MA, USA) and 0.01% geneticin (Life Technologies, Carlsbad, CA, USA). Transient transfections were performed on suspension cells using polyethyleneimine (Polysciences Inc., Warrington, PA, USA). For imaging, HEK-293 cells were cultured in DMEM + GlutaMAX™-1 medium supplemented with 10% w/v FBS, 1% w/v nonessential amino acids, and 1% w/v antibiotic–antimycotic. Transient transfections were performed on adherent cells in the absence of antibiotic–antimycotic using Metafectene (Biontex, Munich, Germany). Unless stated otherwise, reagents are purchased from Thermo Fischer Scientific.

Flow cytometry

RAJI and HEK-293 cells were harvested for flow cytometry analysis 16 h after transfection with GFP-tagged CD9

(mutants). Single-cell suspensions were blocked in PBS, 1% w/v BSA, and 2% v/v normal human serum for 30 min at 4 °C and subsequently stained for 30 min at 4 °C in the same solution supplemented with 10 $\mu\text{g}\cdot\text{mL}^{-1}$ of the following primary antibodies: anti-CD9 (MEM61; Thermo Fisher Scientific), anti-CD9 (C9BB, a kind gift of M. E. Hemler), or mouse IgG1 (MOIC-21; BioLegend, San Diego, CA, USA). This was followed by 30-min incubation with anti-mouse IgG1-Alexa Fluor 647 (Thermo Fisher Scientific). Stained cells were analyzed using a Cyan flow cytometer (Beckman Coulter, Brea, CA, USA) and FLOWJO software version 10 (Tree Star Inc., Ashland, OR, USA).

Confocal microscopy and image analysis

Sixteen hours after transfection, HEK-293 cells were fixed in 4% v/v paraformaldehyde (PFA) for 20 min and RAJI cells were adhered to poly-L-lysine-coated coverslips and subsequently fixed. Cells were blocked in 3% w/v BSA, 1% w/v filtered human serum, and 10 mM glycine in PBS for 1 h and subsequently stained for 30 min in the same solution supplemented with 10 $\mu\text{g}\cdot\text{mL}^{-1}$ of the following primary antibodies: anti-CD9 (MEM61; Thermo Fisher Scientific) or anti-EWI-F (polyclonal; Thermo Fisher Scientific). This was followed by a 30-min incubation with an appropriate secondary antibody: anti-mouse IgG1-Alexa Fluor 647 or anti-rabbit IgG-Alexa Fluor 647 (both Thermo Fisher Scientific). Samples were then stained with DAPI, washed, and embedded in mowiol. For intracellular staining of EWIF, cells were permeabilized for 10 min in 0.1% Triton X-100 in PBS and all subsequent solutions contained 0.5% w/v saponin. Samples were imaged on a SP8 confocal microscope with a 60 \times water 1.2 NA objective (Leica, Wetzlar, Germany) using appropriate laser lines and settings. Colocalization was analyzed using the Coloc2 application of FIJI, and the other image analysis was performed using CELLPROFILER [92].

Purification of CD9_{HIS-EPEA} for nanobody generation

For large-scale purification of CD9_{HIS-EPEA} A₆ mutant, HEK-293 cells were harvested after 84 h, resuspended using a Dounce homogenizer, and incubated for 1 h at 4 °C in hypotonic buffer [25 mM HEPES/NaOH pH 7.5; 150 mM NaCl; 10 mM MgCl₂; 2 tablets of EDTA-free protease inhibitor cocktail (Roche)]. Membranes were collected by ultracentrifugation (45 min; 37 000 g; 4 °C), resuspended, and incubated for 1 h at 4 °C in hypertonic buffer [25 mM HEPES/NaOH pH 7.5; 1 M NaCl; 10 mM MgCl₂; 1 $\mu\text{g}\cdot\text{mL}^{-1}$ DNase I (Sigma); 2 tablets of EDTA-free protease inhibitor cocktail (Roche)]. Membranes were collected again by ultracentrifugation and solubilized in Buffer A (described above). After ultracentrifugation, the supernatant was applied to Nickel-

Sepharose high-performance beads (GE Healthcare) for batch binding overnight. The Nickel beads were manually packed in a Tricorn column (GE Healthcare) connected to a second Tricorn column, packed with EPEA beads (Thermo Fisher), on an Äkta chromatography system (GE Healthcare). After extensive washing in Buffer B (described above), the protein was eluted with Buffer C (25 mM HEPES/NaOH pH 7.5, 150 mM NaCl, 250 mM Imidazole, 0.025% w/v DDM) directly onto the EPEA column. The second elution from the EPEA column was performed in Buffer D (25 mM HEPES/NaOH pH 7.5, 150 mM NaCl, 2 mM EPEA peptide, 0.025% w/v DDM). The eluted fractions were pooled and concentrated using a 50 kDa MWCO concentrator (Merck Millipore, Burlington, MA, USA). The protein was finally purified using SEC on a Superdex 200 10/300 column (GE Healthcare), previously equilibrated in Buffer B. Pooled fractions were concentrated to 0.4 $\text{mg}\cdot\text{mL}^{-1}$ and used for llama immunization.

Llama immunizations, phage display library construction, and nanobody selections

One llama was subcutaneously injected with purified non-lipidated (A₆) human CD9_{HIS-EPEA} in Buffer B four times over a period of 6 weeks. Forty microgram of protein was used per injection with an interval of 2 weeks between subsequent boost injections. Pre-immune, as well as sera, samples 4 weeks (after 1st boost) and 6 weeks (end of immunization) after the start of immunizations were used to evaluate the presence of immune response. A nanobody library was constructed by QVQ B.V. (Utrecht, the Netherlands), the Netherlands, using the VHH repertoire that was found in peripheral blood lymphocytes (PBLs) of the immunized llama. In summary, total RNA was extracted from PBLs and the cDNA obtained from an RT-PCR was used as template to specifically amplify the DNA sequences encoding the VHHs. VHH fragments, digested with SfiI & BstEII, were ligated into a pUR8100 phagemid vector, and *E. coli* TG1 bacteria were transformed yielding a nanobody phage display library with a size of 1.1×10^8 . Phages obtained from the CD9 library, as well as from already existing libraries obtained from immunizations with CD9-expressing cells, were panned on 1 μg of C-terminal 3Strep-tagged wild-type CD9 (wtCD9-3Strep) immobilized on pre-blocked Streptavidin-coated wells (Pierce™ Streptavidin-Coated High-Capacity Plates, Thermo Scientific) for 2 h at room temperature. Extensive washing with 0.05% v/v Tween/PBS followed, and the remaining bound phages were eluted by an incubation with trypsin (1 $\text{mg}\cdot\text{mL}^{-1}$) for 40 min. A clear amplification in the phage titer over the control was observed in the phages that were eluted from the CD9 library. Therefore, 94 single TG1 colonies were tested in a phage ELISA to confirm specific binding on CD9.

Phage ELISA

Phages from single colonies were produced after superinfection of log-phase 100 μ L TG1 cultures with M13KO7 helper phage, which were further allowed to grow at 37 °C overnight while shaking. wtCD9-3Strep was incubated for 2 h at room temperature on Streptavidin-coated plates (100 ng per well), and CD9-coated wells were blocked with 4% w/v milk in Buffer B for another hour. The overnight bacterial cultures were pelleted by centrifugation at 4600 *g* for 20 min. Both empty and wtCD9-3Strep-containing streptavidin 96-wells plates were incubated with 20 μ L of phage-containing supernatant for 2 h at room temperature in Buffer B supplemented with 2% w/v milk. After extensive washing with 0.05% v/v Tween in PBS, bound phages were detected with horseradish peroxidase-coupled anti-M13 antibodies (1 : 10 000 in 2% w/v milk in PBS). Peroxidase activity after addition of 3,3',5,5'-tetramethylbenzidine (TMB; 1-Step Ultra TMB-ELISA, Thermo Scientific) was evaluated after measuring absorbance at 450 nm using a FLUOstar microplate reader (BMG LabTech, Ortenberg, Germany). The clones showing binding only on the CD9-coated wells were sent for sequencing with the M13 forward primer (Macrogen, Amsterdam, the Netherlands) and the ones that had unique sequences were further characterized.

Nanobody production and purification

Nanobody was produced as described before [93]. For the first characterization steps, nanobody was produced from the phagemid vector pUR8100-myc-His. The DNA sequence of nanobody clone 4C8 was further ligated into an in-house modified pET28 expression vector using SfiI and BstEII sites in order to introduce a C-terminal free cysteine. In brief, expression was induced in YT2x/ampicillin (100 μ g·mL⁻¹; Sigma-Aldrich BV, Saint Louis, MO, USA) cultures of log-phase (OD₆₀₀ 0.5–0.6) *E. coli* BL-21 Codon Plus (DE3)-RIL bacteria (Agilent Technologies Inc., Santa Clara, CA, USA) transformed with nanobody-encoding plasmids, by addition of IPTG (Thermo Scientific) at a final concentration of 1 mM. The cultures were further allowed to grow overnight at 25 °C under continuous shaking. The periplasmic fraction of the bacterial cultures was applied to either Ni-NTA beads (Qiagen, Hilden, Germany) or anti-EPEA beads (home-made) and incubated for 1 h at 4 °C on an overhead rotator. For His-tagged nanobodies, beads were washed with 10-bed volumes of 15 mM imidazole in PBS, pH 7.0, before elution with 300 mM imidazole in PBS, pH 7.4. For EPEA-tagged nanobodies, PBS was used for washing and 20 mM Tris, pH 7.0, and 2 M MgCl₂ was used for elution instead. Overnight dialysis in SnakeSkin Dialysis Tubing (10K MWCO; Thermo Scientific) against PBS followed. All samples were analyzed with 15% SDS/PAGE to determine

their purity. Pure nanobodies were stored at –20 °C until further use.

Site-directed conjugation of nanobody

Nanobody 4C8cysEPEA was conjugated at its C-terminal cysteine with Alexa Fluor 647 C2 Maleimide (Life Technologies; Thermo Fisher Scientific Inc, Breda, the Netherlands). For that, purified protein sample was buffer exchanged to 5 mM ethylenediaminetetraacetic acid (EDTA) in PBS, pH 8.0 (Sigma-Aldrich BV), using Zeba Spin Desalting Columns (7K MWCO; Life Technologies; Thermo Fisher Scientific Inc). Disulfide bonds were reduced after a 15-min incubation at room temperature with a final concentration of 20 mM Tris(2-carboxyethyl) phosphine hydrochloride (TCEP) in 50 mM Tris/HCl, pH 8.0 (Sigma-Aldrich BV). Afterward, the buffer was exchanged to 0.4 mM EDTA in PBS, pH 7.5, using Zeba column and sample concentration was adjusted to 1 mg·mL⁻¹. Protein samples were mixed with Alexa Fluor 647 C2 Maleimide at a molar ratio of 1 : 4 and incubated overnight at 4 °C on an overhead rotator. Finally, excess of nonreacted free dye was removed from the samples using consecutive Zeba columns conditioned with PBS, until the amount of free dye was below 10% of the total. Conjugates were analyzed on a 15% SDS/PAGE, and the amount of free dye was determined. Absorbance at 280 and 650 nm was measured using a NanoDrop spectrophotometer (Thermo Fisher Scientific Inc), and the degree of conjugation was calculated. All conjugates were stored at 4 °C and tested for binding CD9 prior to use.

Determination of nanobody binding affinity

To determine the binding affinity of nanobody 4C8 on CD9, several strategies were followed. Binding on purified protein was carried on wtCD9-3Strep captured via the Strep-tag on preblocked Streptavidin-coated wells (either in an 8-well strip format; Pierce™ Streptavidin-Coated High-Capacity Plates, Thermo Scientific, or 96-well plate format; NUNC Immobilizer Streptavidin Plates, Thermo Scientific). In all cases, 100 ng of wtCD9-3Strep in Buffer B was added in each well and incubated overnight at 4 °C. The following day, wells were rinsed twice with Buffer B and blocked with 4% w/v milk in Buffer B for 1 h at room temperature before incubation with the nanobodies. Binding affinity assays were also performed on HeLa cells in 96-well flat-bottomed Nunc Nunclon plate (Thermo Scientific Nalgene, Rochester, NY, USA). Two days prior to starting the assay, cells were seeded at a concentration of 4000 cells/well in DMEM supplemented with 10% FBS and 1% Penicillin/Streptomycin (Sigma-Aldrich BV) and kept at 37 °C, 5% CO₂. On the day of the assay, growth medium was replaced with binding buffer (1% BSA and

25 mM HEPES, pH 7.2, in DMEM without phenol red) and binding was carried out at 4 °C. The target (either purified CD9 or CD9 on cells) was incubated with serial dilutions of nanobodies for 2 h in duplicate. When purified protein was used as the target, nanobodies were diluted in 2% w/v milk in Buffer B. In the case of cells, nanobodies were diluted in binding buffer. When not directly fluorescent nanobodies were used, bound proteins were detected by incubation with rabbit anti-VHH antibody (1 : 1000 in 2% w/v milk in PBS; clone k1216, QVQ B.V.) for 1 h, followed by 1-h incubation with goat anti-rabbit IRDye 800CW (1 : 1000 in 2% w/v milk in PBS; LI-COR Biosciences) at room temperature in the dark. For cell-binding assays, cells were fixed with 2% w/v paraformaldehyde in PBS (PFA) for 10 min and a subsequent incubation with 4% w/v PFA for another 10 min, prior to the incubation with the detecting antibodies. Finally, wells were rinsed three times with PBS and bound proteins were visualized by detection of fluorescence with the Odyssey® Infrared Imager. The 800-nm channel was used for IRDye 800CW or 700-nm channel for Alexa Fluor 647 detection. Fluorescent intensities were plotted (mean \pm SD) over protein concentration using the GRAPHPAD PRISM 7 software (GraphPad Software). Apparent binding affinity (K_D) of the different proteins was determined by nonlinear regression curve fitting for one-site-specific binding.

dSTORM microscopy

RAJI cells overexpressing GFP-tagged CD9 (mutants) were harvested 16 h after transfection, blocked on ice in 2% v/v filtered human serum, and 10 mM glycine in PBS for 30 min and stained on ice with an Alexa Fluor 647-conjugated anti-CD9 4C8Nb for 45 min. Stained cells were seeded on poly-L-lysine-coated 25-mm-round coverslips (#1.5 Micro Cover Glass; Electron Microscopy Sciences, Hatfield, PA, USA) and fixed with 0.1% w/v glutaraldehyde, 4% v/v PFA in 0.2 M phosphate buffer pH 7.4 for 30 min. After thorough washing, remaining reactivity of the fixatives was quenched by a 30-min incubation with 100 mM glycine and 100 mM NH₄Cl in PBS. After another extensive wash, coverslips were mounted in a custom-made low-drift magnetic sample holder. Cells were imaged in 1 ml of OxEA buffer [94]. dSTORM microscopy was performed on a custom-build low-drift inverted microscope setup, equipped with a nanometer resolution xyz piezo stage (PI nano P-545.3R7 Piezo System; Physik Instrumente, Karlsruhe, Germany). In the excitation path, spatially overlapping 1000 mW 639 nm (Genesis MX STM OPS Laser System; Coherent, Santa Clara, CA, USA) and 100 mW 405 nm (OBIS LX Laser System; Coherent) laser light sources were expanded and focused at the back focal plane of the imaging objective (APON 60XOTIRF/1.49 OIL; Olympus America Inc., Center Valley, PA, USA). Emission light was focused (f:175 mm achromatic, Newport,

PAC061AR.14, Irvine, CA, USA) on a scientific CMOS camera (ORCA-Flash4.0 V2; Hamamatsu, Hamamatsu City, Japan). All of the instruments were controlled by custom-written software in MATLAB (MathWorks Inc., Natick, MA, USA)

Imaging was performed in wide-field illumination mode. During data acquisition, sample plane excitation power densities of ~ 1.8 – 5.0 kW·cm⁻² were used for the 639-nm laser. Optionally, for back pumping purposes, simultaneous excitation with the 405 nm light source was used at gradually increasing excitation power densities up to maximum of 0.05 kW·cm⁻² in the sample plane. Typically, 50 000 frames were acquired in a region of interest (ROI) of 300 \times 300 pixels with a pixel size of 0.111 μ m at an exposure time of 10 ms.

Image reconstruction and data analysis

Data sets were analyzed with FIJI IMAGE J 1.52g and the analysis module THUNDERSTORM [95]. A detection threshold of 300 photons was used, and typical uncertainty mode values were 20 nm for the 639 channel. Images were reconstructed using the averaged shifted histograms method, with a rendering pixel size of 10 nm. Software drift correction (THUNDERSTORM) was applied based on cross-correlation. The output of THUNDERSTORM, a data file containing the filtered localizations, was further analyzed by the DBSCAN cluster algorithm in R [61,96]. Based on previous research [17], an ϵ -value of 50 nm and a minpts of 5 were chosen. To validate these parameters, an ϵ -value of 25 and 75 nm and a minpts of 3 and 10 were also tested, which yielded similar conclusions. Visualization and data fitting were performed using PRISM5 (GraphPad).

Statistics

Quantification of flow cytometry and (super-resolution) microscopy is based on at least three independent experiments. Results are expressed as means \pm SEM and compared using a Friedman test followed by Dunn's multiple comparison testing. To assess whether DBSCAN clustering parameters were affected by lipidation in a density-independent way, a regression model was fitted on the pooled data from all mutants combined for log # localizations per cluster versus log localizations per μ m² and logit % nonclustered localizations versus log localizations per μ m². The residuals of these regressions for the different CD9 constructs were then compared using ANOVA analysis. Quantification of immunoprecipitation of EWI-F and EWI-2 is based on at least three independent experiments. Results are expressed as means \pm SEM and compared using a one-way ANOVA test followed by Bonferroni's multiple comparison testing. Statistical analysis was carried out in PRISM5 (GraphPad) or R. Statistical significance was defined as * $P \leq 0.05$, ** $P \leq 0.01$, and *** $P \leq 0.001$.

Acknowledgements

We thank W. Hemrika (U-Protein Express B.V.) for HEK cell culture, Z. Szabo (U-Protein Express B.V.) and QvQ for llama immunization and phage library construction, B. Joosten (RIMLS, Nijmegen) for assistance on the dSTORM microscopy, and M. Hemler (Harvard Medical School) for providing the C9BB antibody. This work has been supported by the Netherlands Organization for Scientific Research (NWO): the Institute of Chemical Immunology (project 024.002.009) to AJRH, ABS, and PG, the Radboud PhD grant to IMNW, the NWO Fund NCI Technology Area (project 731.015.201) to PMPBH and PG, VIDI (project 864.11.006) to ABS, and the large-scale proteomic facility Proteins@Work (Project 184.032.201) embedded in the Netherlands Proteomics Centre to AJRH. We acknowledge funding support from the Dutch Cancer Society (KUN2014-6845) to ABS, and the European Research Council: Consolidator Grant (project 724281) to ABS and Advanced Grant (project 787241) to PG.

Conflict of interest

The authors declare no conflict of interest.

Author contributions

VN, SD, ABS, and PG designed the project. VN, SD, JG, and RNPR performed cloning and site-directed mutagenesis. VN and RNPR carried out membrane-protein purification. TPW and MW performed the mass spectrometry measurements and analyzed the data. RNPR carried out quantitative analysis. VN and SH screened initial constructs of lipidation mutants. KTX selected, purified, and conjugated the 4C8 nanobody. SD and JKK performed microscopy imaging and flow cytometry analysis. SD and IMNW analyzed super-resolution microscopy data. PMPBH, AJRH, ABS, and PG provided project guidance. VN, SD, ABS, and PG discussed the results and wrote the manuscript with input from the other authors.

References

- Jiang H, Zhang X, Chen X, Aramsangtienchai P, Tong Z & Lin H (2018) Protein lipidation: occurrence, mechanisms, biological functions, and enabling technologies. *Chem Rev* **118**, 919–988.
- Ko P & Dixon SJ (2018) Protein palmitoylation and cancer. *EMBO Rep* **19**, e46666.
- Daniotti JL, Pedro MP & Valdez Taubas J (2017) The role of S-acylation in protein trafficking. *Traffic* **18**, 699–710.
- Greaves J & Chamberlain LH (2007) Palmitoylation-dependent protein sorting. *J Cell Biol* **176**, 249–254.
- Ernst AM, Toomre D & Bogan JS (2019) Acylation – a new means to control traffic through the Golgi. *Front Cell Dev Biol* **7**, 109.
- Zaballa M & Van Der Goot FG (2018) The molecular era of protein S-acylation: spotlight on structure, mechanisms, and dynamics and dynamics. *Crit Rev Biochem Mol Biol* **53**, 420–451.
- Jennings BC & Linder ME (2012) DHHC protein S-acyltransferases use similar ping-pong kinetic mechanisms but display different Acyl-CoA specificities. *J Biol Chem* **287**, 7236–7245.
- Greaves J, Munro KR, Davidson SC, Riviere M, Wojno J, Smith TK, Tomkinson NCO & Chamberlain LH (2017) Molecular basis of fatty acid selectivity in the zDHHC family of S-acyltransferases revealed by click chemistry. *Proc Natl Acad Sci USA* **114**, E1365–E1374.
- Rana MS, Kumar P, Lee C-J, Verardi R, Rajashankar KR & Banerjee A (2018) Fatty acyl recognition and transfer by an integral membrane S-acyltransferase. *Science* **359**, eaao6326.
- Levental I, Simons K, Coskun U, Lingwood D & Grzybek M (2010) Palmitoylation regulates raft affinity for the majority of integral raft proteins. *Proc Natl Acad Sci USA* **107**, 22050–22054.
- Lorent JH, Diaz-Rohrer B, Lin X, Spring K, Gorfe AA, Levental KR & Levental I (2017) Structural determinants and functional consequences of protein affinity for membrane rafts. *Nat Commun* **8**, 1219.
- Blaskovic S, Blanc M & Van Der Goot FG (2013) What does S-palmitoylation do to membrane proteins? *FEBS J* **280**, 2766–2774.
- Joseph M & Nagaraj R (1995) Conformations of peptides corresponding to fatty acylation sites in proteins. A circular dichroism study. *J Biol Chem* **270**, 19439–19445.
- Abrami L, Kunz B, Iacovache I & van der Goot FG (2008) Palmitoylation and ubiquitination regulate exit of the Wnt signaling protein LRP6 from the endoplasmic reticulum. *Proc Natl Acad Sci USA* **105**, 5384–5389.
- Yáñez-Mó M, Barreiro O, Gordon-Alonso M, Sala-Valdés M & Sánchez-Madrid F (2009) Tetraspanin-enriched microdomains: a functional unit in cell plasma membranes. *Trends Cell Biol* **19**, 434–446.
- Rubinstein E, Le Naour F, Lagaudrière-Gesbert C, Billard M, Conjeaud H & Boucheix C (1996) CD9, CD63, CD81, and CD82 are components of a surface tetraspan network connected to HLA-DR and VLA integrins. *Eur J Immunol* **26**, 2657–2665.

- 17 Zuidscherwoude M, Göttfert F, Dunlock VME, Figdor CG, van den Bogaart G & van Spriel AB (2015) The tetraspanin web revisited by super-resolution microscopy. *Sci Rep* **5**, 12201.
- 18 Zuidscherwoude M, de Winde CM, Cambi A & van Spriel AB (2014) Microdomains in the membrane landscape shape antigen-presenting cell function. *J Leukoc Biol* **95**, 251–263.
- 19 van Deventer SJ, Dunlock V-ME & van Spriel AB (2017) Molecular interactions shaping the tetraspanin web. *Biochem Soc Trans* **45**, 741–750.
- 20 Hemler ME (2005) Tetraspanin functions and associated microdomains. *Nat Rev Mol Cell Biol* **6**, 801–11.
- 21 Berditchevski F, Odintsova E, Sawada S & Gilbert E (2002) Expression of the palmitoylation-deficient CD151 weakens the association of alpha 3 beta 1 integrin with the tetraspanin-enriched microdomains and affects integrin-dependent signaling. *J Biol Chem* **277**, 36991–7000.
- 22 Seehafer JG, Tang SC, Slupsky JR & Shaw AR (1988) The functional glycoprotein CD9 is variably acylated: localization of the variably acylated region to a membrane-associated peptide containing the binding site for the agonistic monoclonal antibody 50H.19. *Biochem Biophys Acta* **957**, 399–410.
- 23 Levy S, Nguyen VQ, Andria ML & Takahashi S (1991) Structure and membrane topology of TAPA-1. *J Biol Chem* **266**, 14597–14602.
- 24 Delandre C, Penabaz TR, Passarelli AL, Chapes SK & Clem RJ (2009) Mutation of juxtamembrane cysteines in the tetraspanin CD81 affects palmitoylation and alters interaction with other proteins at the cell surface. *Exp Cell Res* **315**, 1953–1963.
- 25 Yang X, Claas C, Kraeft S-K, Chen LB, Wang Z, Kreidberg JA & Hemler ME (2002) Palmitoylation of tetraspanin proteins: modulation of CD151 lateral interactions, subcellular distribution, and integrin-dependent cell morphology. *Mol Biol Cell* **13**, 767–781.
- 26 Mazurov D, Heidecker G & Derse D (2007) The inner loop of tetraspanins CD82 and CD81 mediates interactions with human T cell lymphotropic virus type 1 Gag protein. *J Biol Chem* **282**, 3896–3903.
- 27 Cherukuri A, Carter RH, Brooks S, Bornmann W, Finn R, Dowd CS & Pierce SK (2004) B cell signaling is regulated by induced palmitoylation of CD81. *J Biol Chem* **279**, 31973–31982.
- 28 Simpson PC, Johnson ME, Oelke A, Todd SC, Clark KL & Eilert KD (2004) CD81 associates with 14-3-3 in a Redox-regulated palmitoylation-dependent manner. *J Biol Chem* **279**, 19401–19406.
- 29 Zhu Y, Luo Y, Cao M, Liu Y, Liu X, Wang W, Wu D, Guan M, Xu Q, Ren H *et al.* (2012) Significance of palmitoylation of CD81 on its association with tetraspanin-enriched microdomains and mediating hepatitis C virus cell entry. *Virology* **429**, 112–123.
- 30 Zhou B, Liu L, Reddivari M & Zhang XA (2004) The palmitoylation of metastasis suppressor KAI1/CD82 is important for its motility- and invasiveness-inhibitory activity. *Can Res* **64**, 7455–7463.
- 31 Termini CM, Cotter ML, Marjon KD, Buranda T, Lidke KA & Gillette JM (2014) The membrane scaffold CD82 regulates cell adhesion by altering $\alpha 4$ integrin stability and molecular density. *Mol Biol Cell* **25**, 1560–1573.
- 32 Termini CM, Lidke KA & Gillette JM (2016) Tetraspanin CD82 regulates the spatiotemporal dynamics of PKC α in acute myeloid leukemia. *Sci Rep* **6**, 1–14.
- 33 Levy S (2014) Function of the tetraspanin molecule CD81 in B and T cells. *Immunol Res* **58**, 179–185.
- 34 Tejera E, Rocha-Perugini V, López-Martín S, Pérez-Hernández D, Bachir AI, Horwitz AR, Vázquez J, Sánchez-Madrid F & Yáñez-Mo M (2013) CD81 regulates cell migration through its association with Rac GTPase. *Mol Biol Cell* **24**, 261–273.
- 35 Zimmerman B, Kelly B, McMillan BJ, Seegar TCM, Dror RO, Kruse AC & Blacklow SC (2016) Crystal structure of a full-length human tetraspanin reveals a cholesterol-binding pocket. *Cell* **167**, 1041–1051.e11.
- 36 Jin Y, Takeda Y, Kondo Y, Tripathi LP, Kang S, Takeshita H, Kuhara H, Maeda Y, Higashiguchi M, Miyake K *et al.* (2018) Double deletion of tetraspanins CD9 and CD81 in mice leads to a syndrome resembling accelerated aging. *Sci Rep* **8**, 5145.
- 37 Angeles García-López M, Barreiro O, García-Díez A, Sánchez-Madrid F & Peñas PF (2005) Role of tetraspanins CD9 and CD151 in primary melanocyte motility. *J Invest Dermatol* **125**, 1001–1009.
- 38 Powner D, Kopp PM, Monkley SJ, Critchley DR & Berditchevski F (2011) Tetraspanin CD9 in cell migration. *Biochem Soc Trans* **39**, 563–567.
- 39 Reyes R, Cardeñes B, Machado-Pineda Y & Cabañas C (2018) Tetraspanin CD9: a key regulator of cell adhesion in the immune system. *Front Immunol* **9**, 1–9.
- 40 Miyado K, Yamada G, Yamada S, Hasuwa H, Nakamura Y, Ryu F, Suzuki K, Kosai K, Inoue K, Ogura A *et al.* (2000) Requirement of CD9 on the egg plasma membrane for fertilization. *Science* **287**, 321–324.
- 41 Le Naour F & Boucheix C (2000) Severely reduced female fertility in CD9-deficient mice. *Science* **287**, 319–321.
- 42 Tachibana I & Hemler ME (1999) Role of transmembrane 4 superfamily (TM4SF) proteins CD9 and CD81 in muscle cell fusion and myotube maintenance. *J Cell Biol* **146**, 893–904.
- 43 Charrin S, Latil M, Soave S, Polesskaya A, Chrétien F, Boucheix C & Rubinstein E (2013) Normal muscle

- regeneration requires tight control of muscle cell fusion by tetraspanins CD9 and CD81. *Nat Commun* **4**, 1674.
- 44 Stipp CS, Orlicky D & Hemler ME (2001) FPRP, a major, highly stoichiometric, highly specific CD81- and CD9-associated protein. *J Biol Chem* **276**, 4853–4862.
- 45 Stipp CS, Kolesnikova TV & Hemler ME (2001) EWI-2 is a major CD9 and CD81 partner and member of a novel Ig protein subfamily. *J Biol Chem* **276**, 40545–40554.
- 46 Charrin S, Le Naour F, Oualid M, Billard M, Faure G, Hanash SM, Boucheix C & Rubinstein E (2001) The major CD9 and CD81 molecular partner. Identification and characterization of the complexes. *J Biol Chem* **276**, 14329–14337.
- 47 Umeda R, Nishizawa T & Nureki O (2019) Crystallization of the human tetraspanin protein CD9. *Acta Crystallogr F* **75**, 254–259.
- 48 Charrin S, Manié S, Oualid M, Billard M, Boucheix C & Rubinstein E (2002) Differential stability of tetraspanin/tetraspanin interactions: role of palmitoylation. *FEBS Lett* **516**, 139–144.
- 49 Sharma C, Yang XH & Hemler ME (2008) DHHC2 affects palmitoylation, stability, and functions of tetraspanins CD9 and CD151. *Mol Biol Cell* **19**, 3415–3425.
- 50 Kovalenko OV, Yang X, Kolesnikova TV & Hemler ME (2004) Evidence for specific tetraspanin homodimers: inhibition of palmitoylation makes cysteine residues available for cross-linking. *Biochem J* **417**, 407–417.
- 51 Yang X, Kovalenko OV, Kolesnikova TV, Andzelm MM, Rubinstein E, Strominger JL & Hemler ME (2006) Contrasting effects of EWI proteins, integrins, and protein palmitoylation on cell surface CD9 organization. *J Biol Chem* **281**, 12976–12985.
- 52 Rodenburg RNP, Snijder J, Van De Waterbeemd M, Schouten A, Granneman J, Heck AJR & Gros P (2017) Stochastic palmitoylation of accessible cysteines in membrane proteins revealed by native mass spectrometry. *Nat Commun* **8**, 1280.
- 53 Leney AC & Heck AJR (2017) Native mass spectrometry: what is in the name? *J Am Soc Mass Spectrom* **28**, 5–13.
- 54 von Heijne G (2006) Membrane-protein topology. *Nat Rev Mol Cell Biol* **7**, 909–918.
- 55 Killian JA & von Heijne G (2000) How proteins adapt to a membrane–water interface. *Trends Biochem Sci* **25**, 429–434.
- 56 Yau W-M, Wimley WC, Gawrisch K & White SH (1998) The preference of tryptophan for membrane interfaces. *Biochemistry* **37**, 14713–14718.
- 57 Rose RJ, Damoc E, Denisov E, Makarov A & Heck AJR (2012) High-sensitivity Orbitrap mass analysis of intact macromolecular assemblies. *Nat Methods* **9**, 1084–1086.
- 58 Seehafer JG, Slupsky JR, Tang SC & Shaw ARE (1988) The functional cell surface glycoprotein CD9 is distinguished by being the major fatty acid acylated and a major iodinated cell-surface component of the human platelet. *Biochim Biophys Acta* **952**, 92–100.
- 59 Boucheix C, Benoit P, Frachet P, Billard M, Worthington RE, Gagnon J & Uzan G (1991) Molecular cloning of the CD9 antigen. A new family of cell surface proteins. *J Biol Chem* **266**, 117–122.
- 60 Heilemann M, Van De Linde S, Schüttpehlz M, Kasper R, Seefeldt B, Mukherjee A, Tinnefeld P & Sauer M (2008) Subdiffraction-resolution fluorescence imaging with conventional fluorescent probes. *Angew Chem Int Ed Engl* **47**, 6172–6176.
- 61 Ester M, Hans-Peter K, Jorg S & Xiaowei X (1996) Density-Based Clustering Algorithms for Discovering Clusters. KDD-96 Proceedings 2, pp. 226–231.
- 62 Shipston MJ (2014) Ion channel regulation by protein S-acylation. *J Gen Physiol* **143**, 659–678.
- 63 Adachi N, Hess DT, Kaku M, Ueda C, Numa C & Saito N (2019) Differential S-palmitoylation of the human and rodent β 3-adrenergic receptors. *J Biol Chem* **294**, 2569–2578.
- 64 Espenel C, Margeat E, Dosset P, Arduise C, Le Grimellec C, Royer CA, Boucheix C, Rubinstein E & Milhiet PE (2008) Single-molecule analysis of CD9 dynamics and partitioning reveals multiple modes of interaction in the tetraspanin web. *J Cell Biol* **182**, 765–776.
- 65 Charrin S, Le Naour F, Labas V, Billard M, Le Caer J-P, Emile J-F, Petit M-A, Boucheix C & Rubinstein E (2003) EWI-2 is a new component of the tetraspanin web in hepatocytes and lymphoid cells. *Biochem J* **373**, 409–421.
- 66 André M, Chambrion C, Charrin S, Soave S, Chaker J, Boucheix C, Rubinstein E & Le Naour F (2009) In situ chemical cross-linking on living cells reveals CD9P-1 cis-oligomer at cell surface. *J Proteomics* **73**, 93–102.
- 67 Colin S, Guilmain W, Creoff E, Schneider C, Steverlynck C, Bongaerts M, Legrand E, Vannier JP, Muraine M, Vasse M *et al.* (2011) A truncated form of CD9-partner 1 (CD9P-1), GS-168AT2, potently inhibits in vivo tumour-induced angiogenesis and tumour growth. *Br J Cancer* **105**, 1002–1011.
- 68 Muszbek L, Haramura G, Cluette-Brown JE, Van Cott EM & Laposata M (1999) The pool of fatty acids covalently bound to platelet proteins by thioester linkages can be altered by exogenously supplied fatty acids. *Lipids* **34** (Suppl), S331–S337.
- 69 Higashihara M, Takahata K, Yatomi Y, Nakahara K & Kurokawa K (1990) Purification and partial characterization of CD9 antigen of human platelets. *FEBS Lett* **264**, 270–274.
- 70 Veit M, Herrler G, Schmidt MFG, Rott R & Klenk H-D (1990) The hemagglutinating glycoproteins of

- influenza B and C viruses are acylated with different fatty acids. *Virology* **177**, 807–811.
- 71 Fujimoto T, Stroud E, Whatley RE, Prescott SM, Muszbek L, Laposata M & McEver RP (1993) P-selectin is acylated with palmitic acid and stearic acid at cysteine 766 through a thioester linkage. *J Biol Chem* **268**, 11394–11400.
- 72 Senyilmaz D, Virtue S, Xu X, Tan CY, Griffin JL, Miller AK, Vidal-Puig A & Teleman AA (2015) Regulation of mitochondrial morphology and function by stearoylation of TFR1. *Nature* **525**, 124–128.
- 73 Fukata M, Fukata Y, Adesnik H, Nicoll RA, Brecht DS & Francisco S (2004) Identification of PSD-95 palmitoylating enzymes University of California at San Francisco. *Neuron* **44**, 987–996.
- 74 Adachi N, Hess DT, McLaughlin P & Stamler JS (2016) S-palmitoylation of a novel site in the β 2-adrenergic receptor associated with a novel intracellular itinerary. *J Biol Chem* **291**, 20232–20246.
- 75 Won SJ, Cheung M, Kit S, Martin BR, Joon S, Cheung M, Kit S & Protein BRM (2018) Protein depalmitoylases. *Crit Rev Biochem Mol Biol* **53**, 83–98.
- 76 Duncan JA & Gilman AG (1998) A cytoplasmic acyl-protein thioesterase that removes palmitate from G protein α subunits and p21(RAS). *J Biol Chem* **273**, 15830–15837.
- 77 Tomatis VM, Trenchi A, Gomez GA & Daniotti JL (2010) Acyl-protein thioesterase 2 catalyzes the deacylation of peripheral membrane-associated GAP-43. *PLoS ONE* **5**, e15045.
- 78 Lin DTS & Conibear E (2015) ABHD17 proteins are novel protein depalmitoylases that regulate N-Ras palmitate turnover and subcellular localization. *eLife* **4**, e11306.
- 79 Fukata Y, Dimitrov A, Boncompain G, Vielemeyer O, Perez F & Fukata M (2013) Local palmitoylation cycles define activity-regulated postsynaptic subdomains. *J Cell Biol* **202**, 145–161.
- 80 Eidenmuller J, Fath T, Hellwig A, Reed J, Sontag E & Brandt R (2000) Structural and functional implications of tau hyperphosphorylation: information from phosphorylation-mimicking mutated tau proteins. *Biochemistry* **39**, 13166–13175.
- 81 Rankin CA, Sun Q & Gamblin TC (2005) Pseudo-phosphorylation of tau at Ser202 and Thr205 affects tau filament formation. *Mol Brain Res* **138**, 84–93.
- 82 Van Hoof D, Muñoz J, Braam SR, Pinkse MWH, Linding R, Heck AJR, Mummery CL & Krijgsveld J (2009) Phosphorylation dynamics during early differentiation of human embryonic stem cells. *Cell Stem Cell* **5**, 214–226.
- 83 Goldfinger LE, Han J, Kiousses WB, Howe AK & Ginsberg MH (2003) Spatial restriction of α 4 integrin phosphorylation regulates lamellipodial stability and α 4 β 1-dependent cell migration. *J Cell Biol* **162**, 731–741.
- 84 Benz PM, Blume C, Seifert S, Wilhelm S, Waschke J, Schuh K, Gertler F, Münzel T & Renné T (2009) Differential VASP phosphorylation controls remodeling of the actin cytoskeleton. *J Cell Sci* **122**, 3954–3965.
- 85 Rajan S, Jagatheesan G, Petrashevskaya N, Biesiadecki BJ, Warren CM, Riddle T, Liggett S, Wolska BM, Solaro RJ & Wiczonek DF (2019) Tropomyosin pseudo-phosphorylation results in dilated cardiomyopathy. *J Biol Chem* **294**, 2913–2923.
- 86 Halff EF, Versteeg M, Brondijk THC & Huizinga EG (2014) When less becomes more: optimization of protein expression in HEK293-EBNA1 cells using plasmid titration – a case study for NLRs. *Protein Expr Purif* **99**, 27–34.
- 87 Kremers GJ, Goedhart J, Van Den Heuvel DJ, Gerritsen HC & Gadella TWJ (2007) Improved green and blue fluorescent proteins for expression in bacteria and mammalian cells. *Biochemistry* **46**, 3775–3783.
- 88 Snijder J, Grinfeld D, Bennett A, Makarov A, Agbandje-McKenna M, Denisov E, Heck AJR, van de Waterbeemd M & Damoc E (2014) Defining the stoichiometry and cargo load of viral and bacterial nanoparticles by Orbitrap mass spectrometry. *J Am Chem Soc* **136**, 7295–7299.
- 89 Van De Waterbeemd M, Fort KL, Boll D, Reinhardt-Szyba M, Routh A, Makarov A & Heck AJR (2017) High-fidelity mass analysis unveils heterogeneity in intact ribosomal particles. *Nat Methods* **14**, 283–286.
- 90 Fort KL, Van De Waterbeemd M, Boll D, Reinhardt-Szyba M, Belov ME, Sasaki E, Zschoche R, Hilvert D, Makarov AA & Heck AJR (2018) Expanding the structural analysis capabilities on an Orbitrap-based mass spectrometer for large macromolecular complexes. *Analyst* **143**, 100–105.
- 91 Bern M, Caval T, Kil YJ, Tang W, Becker C, Carlson E, Kletter D, Sen KI, Galy N, Hagemans D *et al.* (2018) Parsimonious charge deconvolution for native mass spectrometry. *J Proteome Res* **17**, 1216–1226.
- 92 Carpenter AE, Jones TR, Lamprecht MR, Clarke C, Kang IH, Friman O, Guertin DA, Chang JH, Lindquist RA, Moffat J *et al.* (2006) Cell Profiler: image analysis software for identifying and quantifying cell phenotypes. *Genome Biology* **7**, R100.
- 93 Roovers RC, Laeremans T, Huang L, De Taeye S, Verkleij AJ, Revets H, de Haard HJ & van Bergen en Henegouwen PMP (2007) Efficient inhibition of EGFR signaling and of tumour growth by antagonistic anti-EGFR nanobodies. *Cancer Immunol Immunother* **56**, 303–317.
- 94 Nahidiazar L, Agronskaia AV, Broertjes J, Van Den Broek B & Jalink K (2016) Optimizing imaging conditions for demanding multi-color super resolution localization microscopy. *PLoS ONE* **11**, 1–18.

- 95 Ovesný M, Křížek P, Borkovec J, Švindrych Z & Hagen GM (2014) ThunderSTORM: a comprehensive ImageJ plug-in for PALM and STORM data analysis and super-resolution imaging. *Bioinformatics* **30**, 2389–2390.
- 96 Campello RJGB, Moulavi D & Sander J (2013) Density-based clustering based on hierarchical density estimates. In *Advances in Knowledge Discovery and Data Mining* (Pei J, Tseng VS, Cao L, Motoda H & Xu G, eds), pp. 160–172. Springer Berlin Heidelberg, Berlin, Heidelberg.
- 97 Lomize MA, Pogozheva ID, Joo H, Mosberg HI & Lomize AL (2012) OPM database and PPM web server: resources for positioning of proteins in membranes. *Nucleic Acids Res* **40**, 370–376.

Supporting information

Additional supporting information may be found online in the Supporting Information section at the end of the article.

Fig. S1. Profiling of CD9 and CD81 wild-type palmitoylation.

Fig. S2. (I) Profiling of CD9 and CD81 mutants having one or three cysteine lipidation-sites. (II) Location of membrane-proximal cysteines in CD81. (III) Quantitative analysis of lipidation occurrence in CD9 and CD81. (IV) Mutants mimicking CD9 lipidation.

Fig. S3. (I) Characterization and labeling of the anti-CD9 nanobody 4C8 for use in super-resolution microscopy. (II) Different ϵ - and minpts-values do not induce differences between samples.

Fig. S4. Lipidation of CD9 does not affect colocalization of CD9 with EWI-F in HEK-293 cells.

Table S1. Sequence of CD9 and CD81 wild-type constructs.

Table S2. Expected native masses of different CD9 and CD81 mutants.